THE EFFECT OF DEFORMATION ON CLUMPED ISOTOPE CONCENTRATION IN CALCITE

A Thesis

by

AHMET UNAL

Submitted to the Office of Graduate and Professional Studies of
Texas A&M University
in partial fulfillment of the requirements for the degree of

MASTER OF SCIENCE

Chair of Committee,	Frederick M. Chester
Co-Chair of Committee,	Andreas K. Kronenberg
Committee Members,	Judith S. Chester
	Berna Hascakir
Head of Department,	Michael Pope

May 2018

Major Subject: Geology

ABSTRACT

The use of clumped isotope analysis in calcite is a rapidly developing and powerful technique for paleothermometry studies in tectonics and environmental sciences. For analysis of isotopes in deformed rocks, there is uncertainty if the deformation of the calcite can reset clumped isotope concentrations, which limits the utility of the method. The goal of this research is to help determine if some typical deformation processes, specifically plastic deformation of calcite at low temperatures (<200 C), can affect clumped isotope concentrations. Seven cores of calcite are deformed experimentally at strain rates 2-4.2x10^{-5} s^{-1}, temperatures from 20 – 400 C, at confining pressure of 150-200 MPa, and to strains of 10-25%. The cores are taken from parent crystals in four different orientations relative to the crystallographic directions of calcite in order to induce different types of deformation. The deformed samples were studied using optical microscopy and electron backscatter diffraction microscopy techniques to identify the types of plastic deformation that operated in each test. Both mechanical *e*-twinning and *r*- and *r*+ slip were successfully activated, and to varying degrees, in the sample suite. Yield strengths observed in the experiments agree well with that expected (based on previous work) for the twin and slip mechanisms identified through microscopy. On the basis of the outcomes of this research, clumped isotope measurements of the parent crystals and the deformed samples will determine if, and which deformation processes affect isotope concentrations. If isotope concentrations remain unchanged by deformation, then the reliability of clumped isotope analysis in deformed rocks will be assured. If deformation resets clumped isotope concentrations, then with further research the method holds great promise to determine the temperature at the time of deformation, which would be a unique capability.

DEDICATION

To Mustafa Kemal Ataturk, who provided government support for students by legislating the code 1416 "act for student scholarship for higher education in foreign countries" in the year of 1929.

ACKNOWLEDGEMENTS

Foremost, I would like to express my sincere gratitude to my advisor and mentor Prof. Frederick Chester for providing the opportunity to work on this project with him. I am grateful for his precious guidance and patient and helping me writing this thesis.

I would like to thank Prof. Andreas Kronenberg specially, who helped and worked with me throughout the experiment series. He extended my knowledge on many topics and especially for this research. I would like to thank Prof. Judith Chester for her contributions and time spent for me. I always liked her enthusiastic and comprehensibly presented teaching style. I also would like to thank to my other committee member Prof. Berna Hascakir.

I would like to thank to Hiroko Kitajima, Jihui Ding, and Guangjian Xu for their help on building data acquisition system for the Ar gas rig. I also thank Tom Stephens who helped me on using the SEM at the Microscopy and Imaging Center.

And my friends in the Geology department, I thank you each other. I have been happy to be among you during my education in College Station.

Finally, thanks to my family, Emine, Nurettin, and Nihat; mother, father and brother of mine. Their existence and boundless support make anything possible.

CONTRIBUTORS AND FUNDING SOURCES

This research was supervised by a thesis committee consisting of Professor Frederick Chester, Professor Andreas Kronenberg, and Professor Judith Chester, faculty members of the Department of Geology and Geophysics and Professor Berna Hascakir, a faculty member of the Department of Petroleum Engineering.

The deformation experiments of this study were conducted on Heard Argon gas pressure apparatus in Handin Rock Deformation Laboratory at the Center for Tectonophysics, Texas A&M University, College Station, Texas. The EBSD work was done in the Microscopy and Imagining Center at Texas A&M University. The funding of graduate study was provided by Turkish Petroleum Corporation (TPAO).

TABLE OF CONTENTS

LIST OF FIGURES

LIST OF TABLES

INTRODUCTION

Clumped isotope geochemistry is a promising and new paleothermometry method in the geosciences. The clumped isotope technique of geothermometry is based on the slight bonding preference of heavy isotopes during crystal growth in calcite and other carbonate minerals. It is known that this preference is a function of temperature at which calcite precipitates, and it may provide information for the growth of calcite grains. The advantage over $\delta^{18}O$ (the abundance ratio of ^{18}O and ^{16}O) geothermometry is that clumped isotope ratios do not depend on global ice/water ratios or salinity of oceans. Besides paleothermometry of oceans, tectonics-related problems also have been studied using the carbonate clumped isotope technique. It can be used to reconstruct time and space relationships between fluid evolution of structural elements (such as folds, faults, and nappes) and regional tectonics. The clumped isotope method may provide constraints on fluid sources of veins filled by carbonates. This method is also used to reveal structural control on cementation and diagenesis within different sections of fault zones. The ability to determine temperature at the time of faulting in carbonates may help the study of shear heating processes during faulting. The method is also a new tool to constrain altimetry of deforming orogenies and thereby help constrain continental tectonic models.

This study will explore potential effects of deformation on clumped isotopes in calcite and their response to different intracrystalline deformation mechanisms of twinning and dislocation glide. In the experiments, single crystals of calcite will be deformed in different orientations under controlled conditions in the Argon gas rig pressure apparatus in the Center for Tectonophysics Laboratory at Texas A&M University. Optical microscopy and electron back-scattering diffraction (EBSD) will be employed to investigate and characterize mechanisms of deformation. Calcite crystals will be prepared and sent for mass spectrometry measurements.

Any changes in clumped isotopes will be studied as a function of deformation conditions and activation of different deformation mechanisms (i.e., twinning and dislocation glide). If the findings of this research show that existing clumped isotopes within a calcite crystal sample are not reset by deformation, then the clumped isotope signature may be interpreted in terms of crystal growth prior to deformation. If my findings show that clumped isotopes change during deformation, then the clumped isotope signature may be interpreted to reflect temperatures at the time of deformation, rather than temperature estimates during earlier geologic events. Most slip systems in calcite are thought to involve slip between carbonate ions (CO_3^{2-}), and therefore by the breaking and reforming of Ca-O bonds. However, few observations bear directly on the atomic-scale deformation processes of dislocation slip and twinning. During such deformation, if the clumped isotopic signature shows no change, only Ca-O bonds have been broken. If the clumped isotopic signature does change, then breaking of C-O bonds is also true.

BACKGROUND

Clumped Isotope Concepts

Isotopes, that have the same number of protons and different numbers of neutrons, are variants of a specific element. The number of neutrons in element's nucleus is not capable of influencing the general chemical properties of the element. However, it results in a change in isotope mass, producing minor differences in bonding strength and zero-point energy levels between light and heavy isotopes of the same element. Isotope fractionation results from these isotope mass differences and is used to attain isotopic features and information of a substance that relate to its specific environment. Isotope geochemistry, in general, is interested in relative and absolute ratios of heavy and light isotopes abundance in geological materials, such as fossils, minerals, and rocks. In isotope geochemistry, delta, δ, and the letter R refer to the relative ratio and absolute ratio, respectively. Mc Kinney et al. (1950) first defined δ as

$$\delta^{18}O = \left\{ \frac{R_{sample}}{R_{standard}} - 1 \right\} \times 1000 \text{ (per mille, ‰)} \quad (1)$$

The unit for a delta value is per mil (‰). The letter R is the absolute ratio of heavy to light isotopes in a sample relative to a standard (reference sample), such as D/H, $^{13}C/^{12}C$, and $^{18}O/^{16}O$. The Vienna Standard Mean Ocean Water (VSMOW) and Vienna Pee Dee Belemnite (VPDB) are two important standards used for hydrogen, oxygen, and carbon isotope measurements.

Researchers use the delta notation (δ) for different applications. For instance, the relative isotope ratios have been employed to reconstruct paleotemperatures dominating in a region in the geological past. Carbonate fossils are an appropriate sample for these estimations owing to isotopic fractionation dependency on formation temperature. Specifically, oxygen fractionation in carbonate fossils is used for paleoclimate estimates (See Equation 2). The oxygen

fractionation relation to environmental temperature stems from an enrichment of light or heavy oxygen in water from which carbonate precipitated.

$$\delta^{18}O = \left\{ \frac{(^{18}O/^{16}O)_{sample}}{(^{18}O/^{16}O)_{stndrd}} - 1 \right\} x \ \ 1000 \text{ (per mille, ‰)} \qquad (2)$$

The enrichment of light or heavy oxygen in an environment depends on evaporation and precipitation. In a warm environment, the water that is rich in light ^{16}O isotopes evaporates first, and oceanic water becomes enriched in ^{18}O isotopes. The opposite is true for condensation of water vapor. In cold environments, such as polar areas, ^{18}O-rich heavy water precipitates first depleting ^{18}O isotopes and resulting in enrichment of light ^{16}O isotopes. This climate-related process has played a significant role in determining paleoclimate patterns. The conventional $\delta^{18}O$ method, however, has limitation regarding oxygen isotope composition in water and carbonate material. Since the method depends on isotope masses, some factors such as salinity of ocean water and global ice volume must be known to make reliable estimates (Affek, 2012). This indirect measurement of $\delta^{18}O$ makes the method troublesome.

The clumped isotope method was introduced as a new paleothermometer about a decade ago by Ghosh et al. (2006). Clumped isotope thermometry, which is independent of water composition, benefits from temperature dependency of bond making between two heavy isotopes of carbonate and oxygen, ^{13}C and ^{18}O, respectively (Ghosh et al., 2006). This method gives temperature estimates for the past more directly as it does not consider the oxygen isotope composition in water from which carbonate precipitated. Clumped isotope analyses consider the state of ordering of scarce isotopes in earth materials, such as fossils, carbonate rocks and carbonate minerals (Eiler, 2007), and measure the deviation of rare (heavy) isotope abundance in a sample with respect to the standard sample considering targeted rare isotopes as randomly distributed (Affek, 2012). Due to the thermodynamic dependence of heavy isotopes bonding (i.e,

clumping), the concentration of heavy isotopologues in a compound may reflects an environmental temperature of the carbonate system during its precipitation. This relation is explained by Eiler (2007) and depends on the vibrational energy level of heavy isotope bonds; accordingly, the number of heavy isotope substitutions in a compound is directly related to the difference in bond energy levels. The energy level for isotopologues that substituted a single heavy isotope is two times greater than isotopologues that substituted a double heavy isotope. In the Figure 1, the colored horizontal lines represent the energy level of doubly-bonded light isotopes (light-light, XX), doubly-bonded heavy isotopes (heavy-heavy, YY), and light-heavy (XY) isotopes. The energy difference between XX and XY is equal to the energy difference between XY and YY. In other words, energy level is doubled between XX and YY with

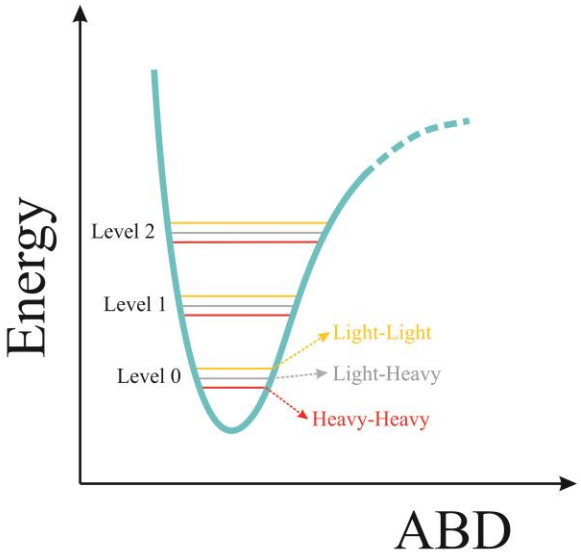

Figure 1. Energy level diagram of a molecular bonding in a plot of bond energy level versus atomic bond distance (ABD). Level 0 is the zero-point energy. The energy values of molecular bonds containing different isotopes are represented by yellow, grey, and red lines.

respect to XX and XY. This relation is defined as the Rule of the Mean (Bigeleisen,1955). The small difference between the vibration energies of heavy and light isotopologues of the same compound leads to a favored partition for the heavy isotope in the compound. This thermodynamically driven increase in the heavy isotope concentration influences the equilibrium constant, *k*.

The isotope exchange reaction below is used to show the effect of favored partitioning of heavy isotopes (As described above, X: light, Y: heavy)

$$2XY = X_2 + Y_2 \quad (3)$$

$$k = [X_2][Y_2] / [XY]^2 \quad (4)$$

Equation (4) gives the *k* for the reaction expressed in (3), for the case when the isotopologues are randomly distributed in a substance (Eiler, 2007). Doubly-substituted Y_2 has lower vibrational energy level (Fig. 1), which indicates increased stability. Accordingly, increasing temperature induces more randomly distributed heavy isotopes in a system. In other words, increasing temperature drives the equilibrium constant *k* closer to the $k_{stochastic}$, by decreasing the doubly-bonded heavy isotope concentration ($[Y_2]$) in the system (Fig. 2).

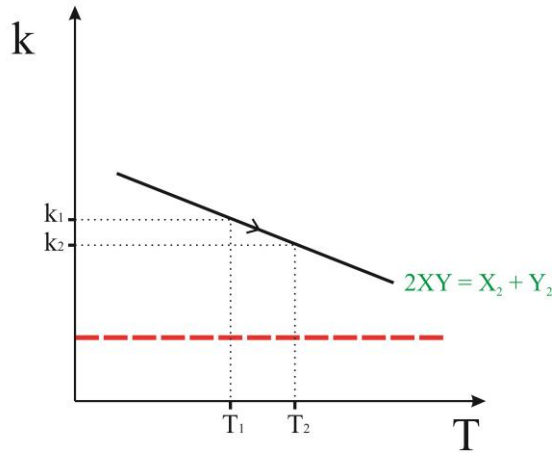

Figure 2. The simplified representation of the relation of equilibrium constant and temperature for an isotope exchange reaction. The dashed red line is the stochastic equilibrium constant.

Clumped isotope geochemistry in carbonate minerals calculates the values of Δ_{47} isotopologues in a material by using the abundances of heavy C-O bonds. The calculation of Δ_{47} is done by first measuring the abundance of heavy CO_2 gas isotopologues extracted from a sample and then comparing the measured values with the values of a stochastically distributed reference material (See Equation 4).

$$\Delta_{47} = \left[\left(\frac{R^{47}_{samp}}{R^{47}_{stoc}} - 1\right) - \left(\frac{R^{46}_{samp}}{R^{46}_{stoc}} - 1\right) - \left(\frac{R^{45}_{samp}}{R^{45}_{stoc}} - 1\right)\right] \times 1000 \quad (5)$$

The equation above uses the abundance ratios of three CO_2 masses, mass-47, mass-46 and mass-45, relative to the most abundant mass-44. In other words, as an example, R^{47}_{samp} is the ratio of mass-47 abundance to mass-44 abundance in a measured sample. This is the same for R^{46}_{samp} and R^{45}_{samp}. In the same way, R^{47}_{stoc}, R^{46}_{stoc}, and R^{45}_{stoc} are the abundance ratios in the randomly distributed sample. The calculation of the denominators is different than the numerators.

$$R^{47}_{stoc} = 2xR^{13}xR^{18} + 2xR^{17}xR^{18} + R^{13}x(R^{17})^2$$

$$R^{46}_{stoc} = 2xR^{18} + 2xR^{13}xR^{17} + (R^{17})^2$$

$$R^{45}_{stoc} = R^{13} + 2xR^{17}$$

In these expressions, R^{13}, R^{17}, and R^{18} are the ratios of mass: $^{13}C/^{12}C$, $^{17}O/^{16}O$, $^{18}O/^{16}O$ respectively (Eiler, 2007; Dennis and Schrag, 2010; Affek, 2012). In most cases, $^{13}C^{18}O^{16}O$, the most abundant isotopologue of mass-47 is used for analyses since it possesses 97% of all ^{13}C-^{18}O bonds of the CO_2. The other two isotopologues of mass-47, which are $^{12}C^{17}O^{18}O$ and $^{13}C^{17}O_2$, do not have significant influences in the calculation (Eiler and Schauble, 2004).

Clumped Isotopes Studies

Recently, researchers have been using the clumped isotope method to establish better temperature proxies that independent from water content of carbonate rock. Even though the calibration research is still underway, the method seems very promising to scientists in terms of accuracy and reliability.

Ghosh et al (2006) and Eiler (2007) published comprehensive papers explaining the clumped isotope concept, its applications, and calibration tests. Eiler then published another paper about the clumped isotope thermometry for paleoclimate reconstruction studies (Eiler, 2011). Finnegan et al. (2011) focused on the glaciation during Ordovician- Silurian. Suarez et al. (2011) studied the multiple isotopologue signature in carbonate paleosol to trace East Asia monsoons. Recently, Lloyd et al. (2017) published a paper about the distance-effects of contact metamorphism environments on calcite and dolomite and their clumped isotope signatures. They found that after the intrusion in the host rock occurred, intracrystalline atomic reordering processes dominated in the aureole and producing a uniform Δ_{47} value of calcite. The altimetry history of the Tibet region was investigated and recalculated by Quade et al. (2011). Eagle et al. (2011) published a paleobiology paper that presents a calculation using clumped isotope thermometry that estimates the body temperature of Jurassic sauropods varied between 36°C and 38°C. Dennis and Schrag (2010) worked on clumped isotopes in terms of diagenetic alteration indicators in carbonatites. Swanson et al. (2012) studied temperatures of faulting and fault-fluids using the clumped isotope technique. Huntington et al. (2015) explained the use of clumped isotope thermometry to explain aspects of continental tectonics and paleoelevation reconstructions. Luetkemeyer et al. (2016) investigated paleofluid sources at 3 km depth along

the active trace of the San Andreas fault by using the clumped isotope method on carbonate veins recovered from the San Andreas Fault at Depth (SAFOD) borehole near Parkfield, Ca.

Calcite Deformation Studies

Calcite mineral and other calcite-bearing carbonate rocks have been studied carefully and widely in different fields by numerous researchers for the last century. These studies, including field and laboratory, investigations have revealed key information about mineralogy, and the timing and temperature of formation, deformation, and diagenesis. In general, deformation of single crystals of calcite can occur by twin and dislocation glide on specific crystallographic slip systems during deformation under an applied stress. This process involves the breaking of atomic bonds. The activation of and train produced by the activation of a particular twin or dislocation glide system depends on several factors: the amount and direction of applied force, ambient temperature during deformation, purity of calcite, and density of defects.

For better comprehension of the subject, some terms and nomenclatures need to be clarified here. Miller-Bravais indices, (hkil), are used in this study to describe a particular crystallographic plane or direction within calcite. All planer and directional Miller-Bravais indices are based on the hexagonal structural calcite unit cell (e.g., De Bresser, 1991). The expression of "sense of slip" or "sense of twinning" represents a direction of an upper-moving section of a crystal after deformation. In case where the upper section slips and moves towards the *c* crystallographic axis then the sense is defined as a positive "+" sense-of-slip; if this movement is away from the *c*-axis, it is called negative sense-of-slip (Turner et al. 1954).

Turner (1954) studied deformation twinning on $\{10\bar{1}4\}$ and $\{01\bar{1}2\}$ and calculated the critical resolved shear stress values for different planes. Turner et al. (1954) followed this work by conducting the very first systematic and remarkable investigation of calcite deformation.

They used cylindrical samples from calcite crystals that were cut in different crystallographic orientations. Compression and extension experiments were performed at temperatures from 20°C to 400°C, under 300 MPa, 500 MPa, and 1000 MPa confining pressures. They identified three main deformation mechanisms: (1) negative slip on the *r*-plane $\{10\bar{1}4\}$ in the $<\bar{2}021>$ direction for deformation at temperatures from 20°C to 300°C, (2) negative slip on the *f*-plane $\{01\bar{1}2\}$ in the $<2\bar{2}01>$ direction, and (3) positive-sense twinning on the *e*-plane $\{01\bar{1}8\}$ in the $<40\bar{4}1>$ direction. Torsion experiments on single crystals of calcite at temperatures ranging from 500°C to 800°C were conducted by Griggs et al. (1960). They pointed out that at the temperatures between 500°C and 600°C, the deformation behavior of calcite goes through a transition, illustrated by the stress-strain behavior. They also observed slip on basal plane *c*{0001}at 800°C. Basal slip was confirmed later by other researchers (Turner and Orozco, 1976; De Bresser and Spiers, 1993).

Positive slip on the *r*-plane was suggested by Weiss and Turner (1972). Spiers and Wenk (1980) observed positive slip on the *f*-plane with slip on the *r*-plane in the positive sense. Positive slip on the *r*-plane and negative slip on the *f*-plane twin systems were identified by Borg and Handin (1967) and Paterson and Turner (1970), respectively. De Bresser and Spiers (1990) observed another new *f*-plane slip direction in positive sense: $<10\bar{1}1>$. Friedman and Conger (1964) worked on calcite twin lamellae that developed in deformed gastropod shells. They found that twin lamellae are well-established in grains that were favorably oriented for twinning for the regional stress direction.

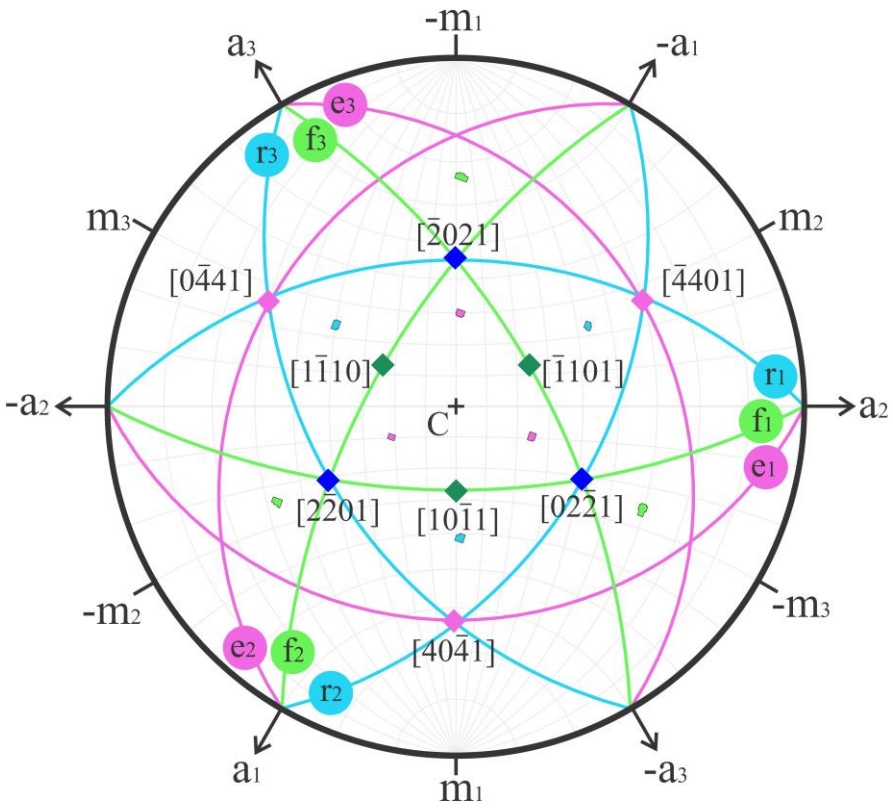

Figure 3. Crystallographic planes, axes and directions for calcite. Upper hemisphere, equal angle projection of crystallographic directions for calcite that exhibits the important planes and directions for deformation by twinning (e) and slip (r, *f)*. The colored planes are three primary planes with the same-colored labels, respectively; planes *e*, *r*, and *f* are represented by pink, blue, and green, respectively. Pink, blue, and green clusters are the EBSD plots of *e*-, *r*- and *f*- plane normals respectively. The plus sign is the *c*-axis. The pink diamond is the twin direction of the *e* plane. The dark blue and dark green are the positive sense slip directions of *r*, and *f* planes respectively.

Calcite displays a number of distinct slip systems, and these systems show different dependencies on stress and temperature (Fig. 3). Generally, e-twinning is activated at the lowest stress levels, on the order of 5-10 MPa critical resolved shear stress, at room temperature (Turner, 1954; De Bresser & Spiers, 1990). Twinning shows only small dependence on temperature with respect to critical resolved shear stress for activation, although the character of twins does change with temperature (e.g., Rowe and Rutter, 1990; Rybacki et al., 2013). The r-slip system, both positive and negative, also are activated at lower stress levels, which are on the

order of 50-120 MPa at room temperature, and show a pronounced reduction in strength with increase in temperature. The f-slip systems require much higher critical resolved stress for activation, and are generally observed only at higher temperatures. For study of the effect of mechanical deformation on clumped isotopes in calcite herein, the focus is on deformation at temperatures of up to 200-400 ˚C, which implies the e-twinning and r-slip systems will be the most significant.

Experimental Approach

A series of experiments can provide the opportunity to test directly whether deformation can change the clumped isotope signatures in calcite. After calcite is deformed under different, controlled conditions, the samples will be investigated under optical and electron backscatter diffraction microscopy (EBSD) in order to determine the crystallographic directions and specific twin and slip systems activated during deformation, estimate strain distribution, and determine specific locations in each deformed calcite crystal for future clumped isotope analysis. After the completion of this work, the deformed samples will be sent to colleagues to carry out mass spectrometry and to determine if the clumped isotope concentrations changed during deformation. By comparing all data from determinations of deformation, temperature conditions, and mass spectrometry measurements, we will be able to determine relationships between changed, post-experiment Δ_{47} values and corresponding deformation conditions (direction, temperature, strain rate).

METHOD

Sample Preparation for Compression Tests

The cylindrical calcite crystal samples were deformed under axial compression. The calcite samples, ranging from 0.3” to 0.8” in length, were cored from four parent calcite crystals in four crystallographic orientations. The four core axis orientations are as follows: parallel to the *c*-axis, normal to the *c*-axis (and parallel to the m-plane), 22° to the *c*-axis, and 68° to the *c*-axis orientation (Fig. 4).

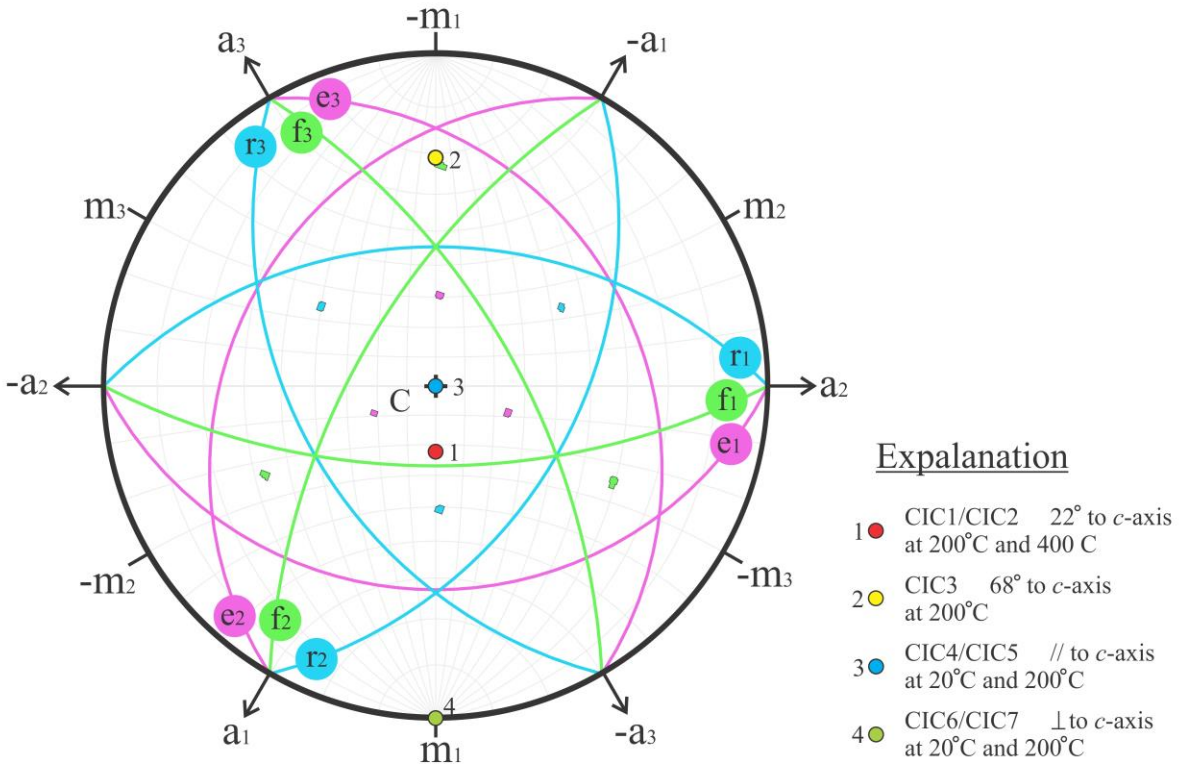

Figure 4. The four orientations of core samples taken relative to the crystallographic directions. The stereographic projection depicting three important planes of calcite (*e*-, *r*- and *f*- planes; pink, blue, green great circles respectively). Pink, blue, and green clusters are the EBSD plots of *e*-, *r*- and *f*- plane normals respectively. The four coring orientations for the sample CIC1 through CIC7 are indicated by small circles with the color assignment as follows, parallel to *c*-axis (blue), normal to *c*-axis (green), 22° to *c*-axis (red), and 68° to *c*-axis (yellow).

The directions of *c*-parallel (0°) and *c*-normal (90°) were selected as being special positions for calcite *c*-axis. The direction of 68° to *c*-axis was selected by the reason of its close angular distance from three crystal planes (*e*, *r*, and *f* planes), and the core-axis direction at 22° to the *c*-axis was chosen because it is the complementary angle to the 68° to *c*-axis-samples. After the cylindrical samples were taken, the ends of the samples were polished with 400 (P800) silicon carbide powder to ensure parallel loading surfaces perpendicular to the core axis.

Deformation Experiments

Seven calcite samples, approximately 1 cm in diameter and 2 cm in length (a ratio of about 1:2, diameter to length), were cored and prepared in the predetermined directions (Fig. 6 and Fig. 7) to activate the common slip systems in calcite. Two samples (CIC1 and CIC2) were cored from the parent crystal Pr1 at 22° to the c-axis. The CIC3 sample was cored from parent crystal Pr2, in the direction 68° to the c-axis (and normal to the direction of CIC1 and CIC2). Two samples (CIC4 and CIC5) were cored parallel to the c-axis in parent crystal Pr3, and two other samples (CIC6 and CIC7) were cored from the Pr4 parent crystal perpendicular to the c-axis.

The polished calcite samples were deformed under triaxial compression parallel to the core axis at a constant confining pressure. Silver jacketing (annealed at 700°C for 24 hours) and Al_2O_3 (aluminum oxide) samplers were used in the seven experiments (Fig. 5).

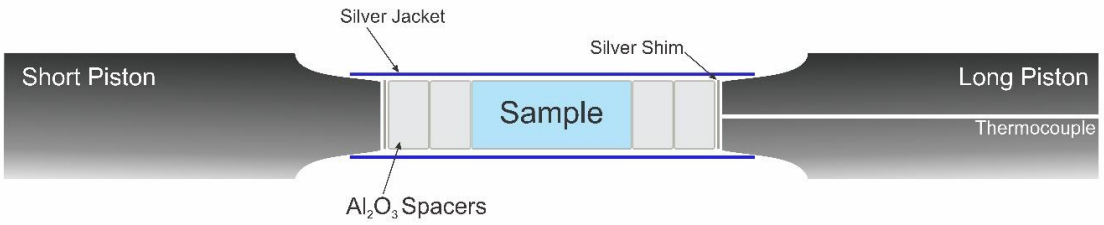

Figure 5. Sample configuration used in the experiment series (not to scale).

The experiments were performed in the water-cooled Argon gas pressure apparatus (Heard and Carter, 1968) in the John Handin Rock Deformation Laboratory at Center for Tectonophysics at Texas A&M University. The deformation tests were conducted at the temperatures of 20°C (room temperature), 200°C, and 400°C, at a constant confining pressure of 200 MPa (with the exception of CIC6 that was at 120 MPa) and at a constant strain rate of $2x10^{-5}$ s^{-1} (Table 1).

Table 1. Matrix of Experiments

Parent Crystal	Sample	Orientation	T (°C)	Pc (MPa)	$\dot{\varepsilon}$ (s-1)
Pr1	CIC1	22° to c-axis	200	200	$2.9x10^{-5}$
	CIC2	22° to c-axis	400	200	$3x10^{-5}$
Pr2	CIC3	68° to c-axis	200	200	$4.2x10^{-5}$
Pr3	CIC4	parallel to c-axis	20	200	$2.4x10^{-5}$
	CIC5	parallel to c-axis	200	200	$2x10^{-5}$
Pr4	CIC6	normal to c-axis	20	150	$2x10^{-5}$
	CIC7	normal to c-axis	200	200	$2.8x10^{-5}$

Mechanical data were collected during each experiment using National Instruments NI 9220, NI 9211 data acquisition modules integrated with LabVIEW software. Differential stress was determined from measurements of differential force and the original diameter of the cores. Axial strain was determined from shortening of the core and the original length, and includes both elastic and permanent deformation. After cooling and depressurization at the end of the experiments, the samples were removed, and the final length was measured directly to determine final, permanent axial strain.

After the experiments, the deformed core samples are inspected to determine the direction of maximum elongation and shear strain perpendicular to the core axis. The samples were then

cut parallel to the core axis and in the direction of elongation and shear using a low-speed, precision saw. One of the two halves was labeled and stored for future mass spectrometry analysis of clumped isotope concentrations. The second half was polished and used to make a petrographic section for optical and electron microscopy; the remaining thin section billet also was retained for mass spectrometry work. A noteworthy point is that attaching the sample half to the glass slide required using acetone to clean both the slide and the cut surface of the sample. The mounted sample was kept warm by a light bulb overnight, to achieve a good bond between the calcite and the glass slide. After affixing the sample half properly, the sample was sliced off leaving a slice of the calcite that was polished, gradually, with progressively finer silicon carbide powder in the sequence 400 GRIT, 600 GRIT, 9.5 μm, 3 μm, 0.3 μm.

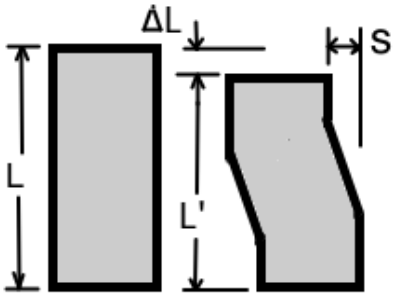

Figure 6. Determination of shear strain for deformed core samples. Axial strain is defined as $\varepsilon = \Delta L/L$, and shear strain $\gamma = S/L'$

An optical microscope and a Nikon COOLSCAN film scanner were employed for observation and photography. The petrographic sections were photographed under plane-polarized light and between crossed polarizers, as well as investigated using an electron scanning microscope to determine the crystallographic orientation of the sample in the different deformation domains. Using the photograph of the section, the permanent axial shortening, and shear strain were determined by direct measurement (Fig. 6).

Sample Preparation and Instrument Information for EBSD

After polishing with silicon carbide powder, the thin sections were polished with Buehler Vibromet 2 vibratory polisher at 40% of amplitude for about 45 minutes. Master Mat 2 polishing suspension 40-6380-064 was used as a polishing liquid during the vibration process. Then, carbon coating was applied over the samples. The EBSD analysis was performed with Fei Quanta 600 FE-SEM field emission scanning electron microscope equipped with 3-axes motorized stage and back-scatter electron detector. The working distance of the detector was 15 mm and the acceleration voltage of the electron beam was 30 kV. The crystallographic orientation data collected during the EBSD were indexed and studied in AZtec 3.2 software by Oxfor Instruments. The locations of the EBSD were selected on different deformation domains in the samples. The number of the EBSD points collected from the samples range 5 to 45 depending on the Kikuchi band quality of that location which is important to index the observation point.

RESULTS

Mechanical Behavior

Seven experiments were completed successfully (Table 2). For all tests the samples were recovered and petrographic sections were prepared so as to allow investigation of the mode of deformation and determine the twin and slip systems activated. Comparing the stress versus strain response of all samples shows significant variation in strength as a function of crystallographic orientation and temperature (Table 2, Fig. 7). As expected, the lowest yield strengths are evident in cores taken normal to the c-axis direction, which favors e-twinning, and greatest strengths are observed for cores taken parallel to the c-axis, which is least favorable for e-twinning. In addition, cores with similar orientations relative to the c-axis show a strength reduction with an increase in temperature, with the notable exception of experiment CIC5 (Table 2, Fig. 7). The mechanical response of experiment CIC5 was so anomalous that the result is considered suspect; however the test procedure, apparatus and data acquisition system functioned properly, so the behavior is attributed to an anomalous core sample.

Table 2. Summary of Experiment Results

Exp. #	Core Axis Orient.	Orientation of Section Cut-Surface	Final Axial Strain-ε_f(%)	Final Shear Strain (γ_f)	Initial Yield Stress (MPa)	Final Yield Stress (MPa)	Quality	EBSD
CIC1	~22°	18° to c-axis, 40° to m_1-plane	24	0.03	24	65	Good	No
CIC2	~22°	12° to c-axis, 62° to m_1-plane	21.7	0.24	~8	~13	Good	No
CIC3	72°	6° to c-axis, 80° to m_1-plane	9	0.05	23	68	Good	Yes
CIC4	3°	4° to c-axis, 72° to m_1-plane	10	0.11	60	89	Good	Yes
CIC5	3°	3° to c-axis, 5° to m_1-plane	8	0.02	172	200	Poor	Yes
CIC6	88°	1° to c-axis, 90° to m_1-plane	24	0.33	7	25	Good	Yes
CIC7	90°	11° to c-axis, 83° to m_1-plane	15	0.19	5	17	Good	Yes

CIC1 and CIC2 Experiments (cored at 22° to c-axis)

The experiments of CIC1 and CIC2 were conducted at the temperatures of 200°C and 400°C. The cores were loaded parallel to the core axis and at 22° to the *c*-axis, at a constant

strain rate of $2x10^{-5}s^{-1}$, under 200 MPa confining pressure. Approximately 20% and 22% strain was achieved in the CIC1 and the CIC2 experiments, respectively (Fig. 7). The stress-strain data for the CIC1 experiment indicates two yield strengths; the first occurs at ~24 MPa and less than 1% strain, the second occurs at ~40 MPa and ~2% strain; similar behavior was reported by De Bresser and Spiers (1997) for this orientation. Unfortunately, the differential force measurements for experiment CIC2 were not properly recorded during the test; however, the conditions at the beginning of the test and at the end of loading were recorded in written records so the strength and strain at the end of the test could be determined (Table 2, Fig. 8). The strengths during deformation are depicted only approximately.

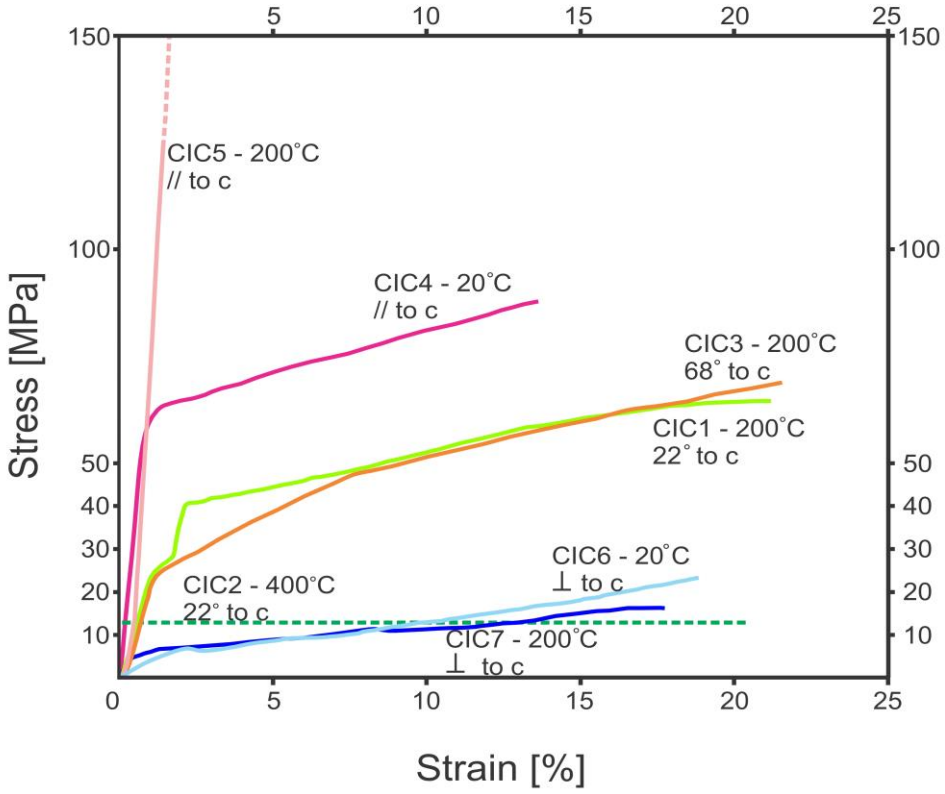

Figure 7. The stress-strain curves for all experiments. Experiment sample number, temperature of deformation, and core orientation are specified for each curve. Other experiment conditions are specified in Tables 1 and 2. As noted in the text, the dashed curve for CIC2 is based only on the final strength because the digital data during deformation was not recovered.

Sample CIC1 displays elastic mechanical behavior until reaching the first yield point at ~24 MPa. Elasto-plastic behavior is displayed between the first and the second yield point. At ~40 MPa there is an abrupt transition to mechanically plastic deformation that is followed by significant strain hardening throughout the rest of the CIC1 deformation experiment. The ultimate stress reached during the experiment is about 70 MPa. Even though, there is no true stress-strain curve for the CIC2 experiment at 400°C temperature, the stress value of the yield point is known as about 13 MPa from the voltage reads changed during the experiment.

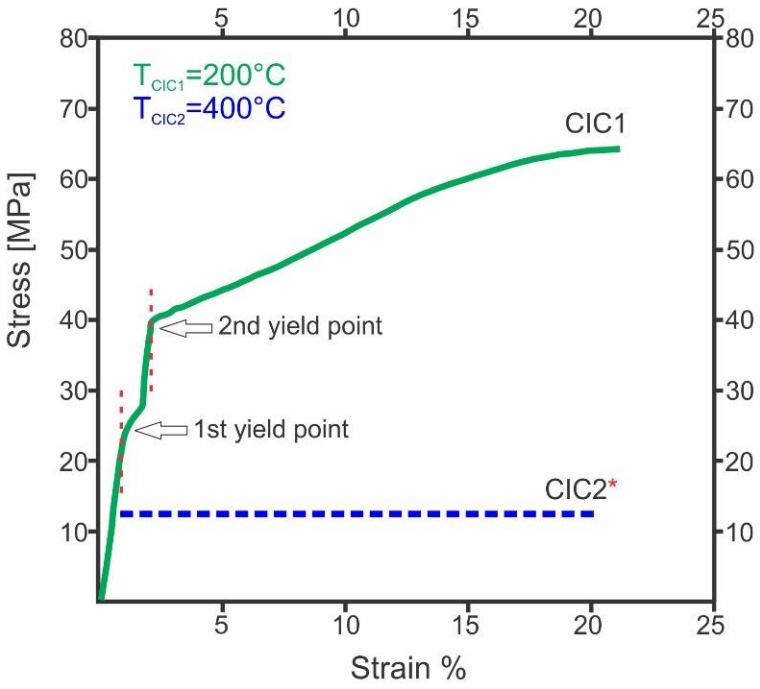

Figure 8. The stress-strain curves for CIC1 and CIC2 experiments. The dashed red lines mark the strain at the two observed yield points of the CIC1 sample. Conditions of each experiment are provided in Tables 1 and 2. As noted in the text, the dashed curve for CIC2 is based only on the final strength because the digital data during deformation was not recovered.

CIC3 Experiment (cored at 68° to c-axis)

The CIC3 sample was deformed at 200°C, a strain rate of $2x10^{-5}s^{-1}$, under a confining pressure of 200 MPa. The orientation of the CIC3 core is 68° to *c*-axis, and perpendicular to the

CIC1 and CIC2 core orientations. Similar to the CIC1 stress-strain curve, the CIC3 experiment shows two yield points (Fig. 9). The first yield point is reached at about 1% strain at ~21 MPa; this is similar to the first yield point of the CIC1 sample. The second yield point occurs little above a strain of 2% at ~27 MPa. The stress-strain relation displays a significant strain-hardening stage after the first yield stress is reached. The final strain reached is about 22% that occurs at 70 MPa.

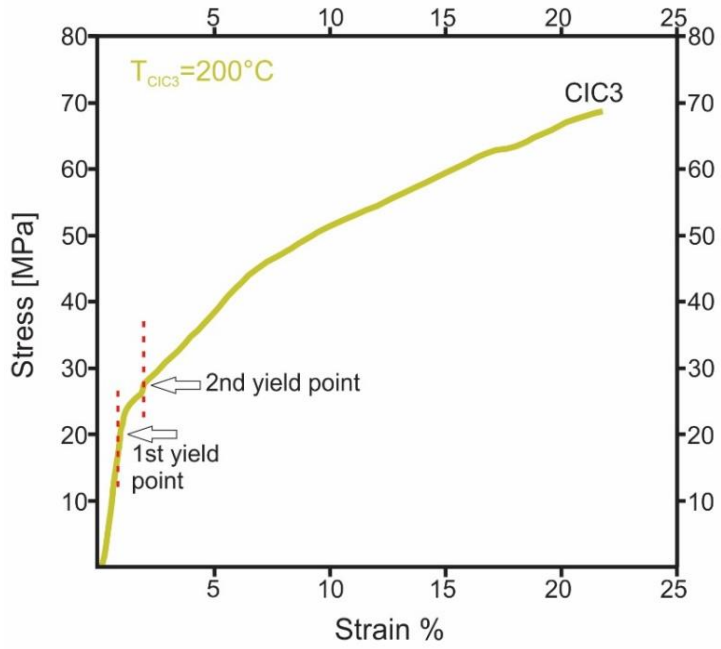

Figure 9. The stress-strain curve for the CIC3 experiment. The dashed red lines mark the strain at the two observed yield points of the sample. Conditions of each experiment are provided in Tables 1 and 2.

CIC4 and CIC5 Experiments (cored parallel to c-axis)

The samples cored parallel the *c*-axis, CIC4 and CIC5, were deformed at 20°C and 200°C respectively (P_c=200 MPa; $\dot{\varepsilon}=2x10^{-1}$ s^{-1}). Different from the CIC1 and CIC2 experiments, which both have two characteristic yield points, CIC4 and CIC5 experiments exhibit one yield point (Fig. 10) at approximately 60 MPa and about 1% strain. The post-yield behavior displays strain-

hardening at a relatively constant rate. In the CIC5 experiment, conducted at 200°C, the yield point is at around 170 MPa with a corresponding ~2% strain. This is the highest yield stress recorded for all deformation experiments, and as previously mentioned, is anomalous. Similar to the CIC4 experiment, the CIC5 sample also shows strain hardening at a relatively constant rate (Fig. 10).

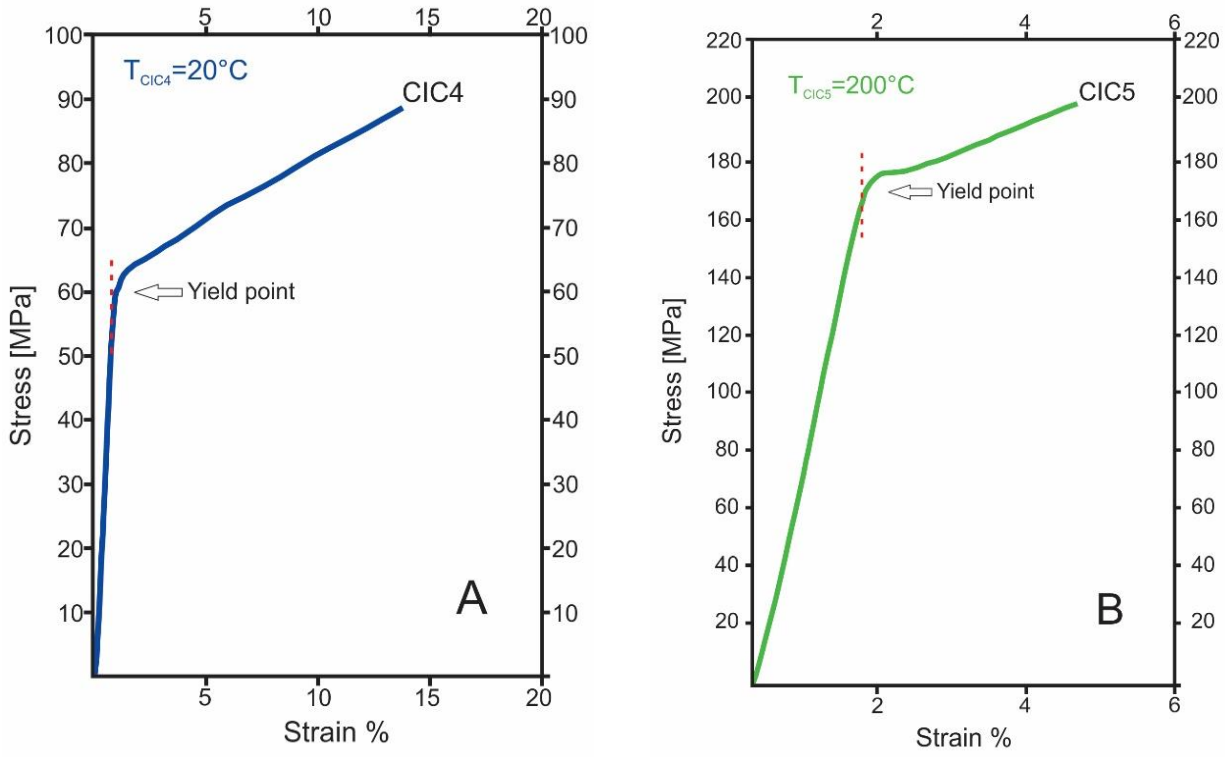

Figure 10. The stress-strain curves for the CIC4 and CIC5 experiments. The dashed red lines mark the strain at the observed yield point for each sample. Conditions of each experiment are provided in Tables 1 and 2.

CIC6 and CIC7 Experiments (cored normal to c-axis)

The calcite samples cored normal to the *c*-axis (CIC6 and CIC7) were deformed at a strain rate of $2x10^{-5}s^{-1}$, a constant confining pressure of 150 MPa and 200 MPa, and at temperatures of 20°C and 200°C, respectively. Experiment CIC6 displays two yield points (Fig. 11). The first yield point occurs at ~7 MPa and ~2% strain. The second yield point occurs at ~9 MPa and ~6%

strain. Like all the other experiments (except CIC2), the CIC6 also displays a strain-hardening stage after the second yield point.

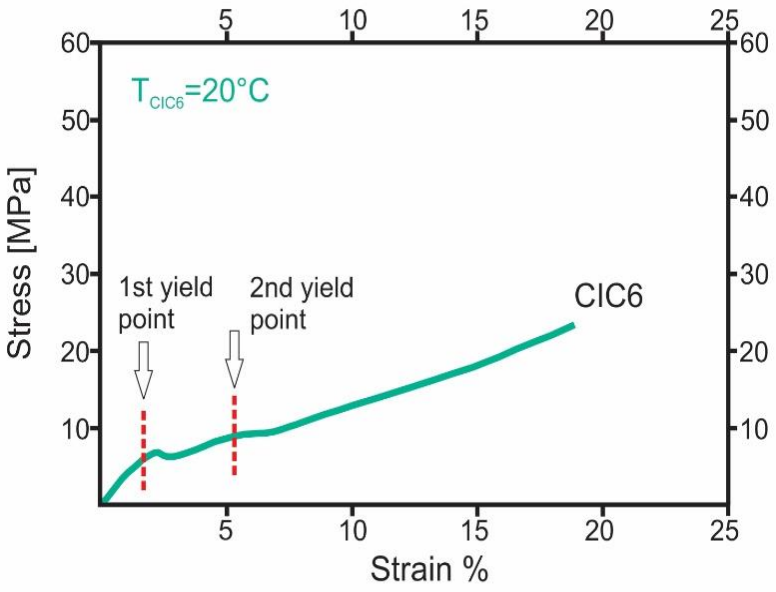

Figure 11. The stress-strain curve of the CIC6 experiment. The dashed red lines mark the strain at the two observed yield points of the sample. Conditions of each experiment are provided in Tables 1 and 2.

In the CIC7 experiment, only stress data signals were collected. Strain data were not obtained because of a malfunction in the displacement transducer (DCDT); the total strain at the end of the experiment, however, could be determined from written records (Fig. 7). The variation in stress during the test allows identification of two yield points. The first yield point occurred at ~5 MPa and the second at about 14 MPa, followed by softening and then hardening to a final strength of 17 MPa. A similar behavior was observed by De Bresser and Spiers (1997) for samples at similar orientations, and was interpreted to reflect the activation of twin gliding at the first yield point, and activation of dislocation glide at the second yield point.

The CIC6 and the CIC7 samples have the same crystallographic orientation so the activated twin and slip systems during axial loading are expected to be similar except for the effect of

temperature. There is some uncertainty in the direct comparison of yield points, however, because of confining pressure differences (150 MPa for CIC6 and 200 MPa for CIC7) and core length differences (the CIC6 sample is ~40% longer than the CIC7 sample) for the two experiments.

Observations

Mode of Failure

The Mode of failure for the samples varies primarily with the crystallographic orientation. The two samples cored and deformed at 22° to the c-axis (CIC1 and CIC2) and at 200°C and 400°C, display relatively similar features. Both activate three sets of twin, and under crossed-polarized light zones of different degrees of extinction indicating either the original crystal has zones of slightly different crystallographic orientation or that the deformation is zoned (domains outlined in yellow in Fig. 12). The intensity of the twins at the ends of the samples likely reflects stress concentrations and strain constraints due to the piston effect (De Bresser and Spiers, 1993). The deformation rotations (internal and external) were determined as ~6° and ~13° from the different extinction angles and twin sets in domains for CIC1 and CIC2, respectively.

CIC3, the sample cored at 68° to *c*-axis had a smaller length to diameter ratio (less than 2:1) than desired for a triaxial deformation test, and smaller when compared to the other test samples of this study. The optical images for CIC3 display less twin and dislocation glide deformation structures when compared to the other samples in this study. Three sets of twins are noted. These twins are inclined at slightly different angles to the applied axial load direction and are visible throughout the section (colored lines; Fig. 12).

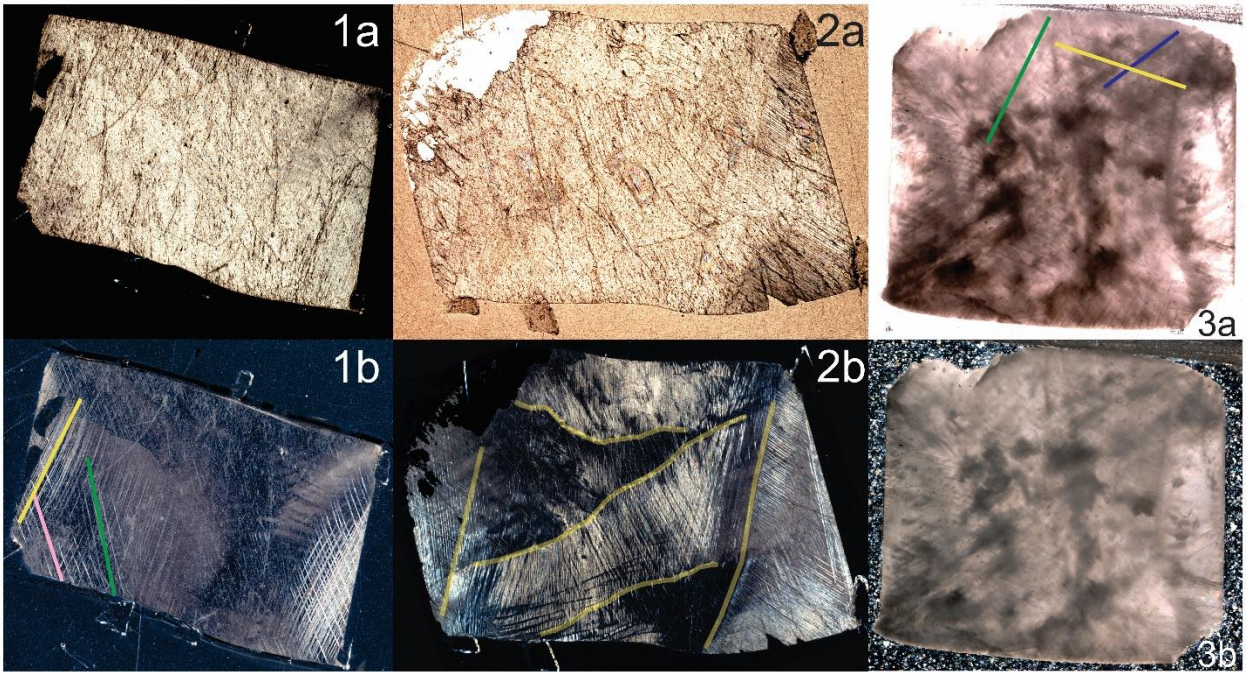

Figure 12. Scanned images of CIC1, CIC2, and CIC3 samples. 1a) Plane-polarized and 1b) cross-polarized light images of the CIC1 sample. The colored lines in (1b) indicate visible twin/slip orientations. 2a) Plane-polarized and 2b) cross-polarized light images of the CIC2 sample. The yellow lines separate the differently oriented twin/slip bands. 3a) Plane-polarized and 3b) cross-polarized light images of the CIC3 sample. The colored lines indicate different possible twin and slip orientations.

The CIC4 sample, cored and compressed parallel to the c-axis at 20°C, shows three sets of twins similar to that noted in the CIC1 and CIC2 samples. The increase in number of twins at the sample ends, seen in the CIC1 and CIC2 samples, also is observed in the CIC4 section. Clear, parallel deformation structures at multiple orientations are observed in the central portion of the CIC4 sample; these likely represent twin planes or slip bands, and are more visible under plane-polarized light (Fig. 13).

The CIC5 section was also cored and compressed parallel to the c-axis similar to CIC4, but was deformed at 200°C. This sample does not show widespread, parallel deformation features produced by twinning or slip, which is unexpected given the significant increase in temperature

of deformation (e.g., Turner, 1954). The CIC5 sample displays irregular microstructures and the original outer shape of the sample is preserved. The lack of through-going deformation features and the anomalous high strength may indicate that the starting sample was not homogeneous, i.e., not a single crystal. Figure 13 shows that a small part of the crystal is distinguishable from a larger part by a boundary that looks more like a crack or grain boundary surface rather than a planar twin or slip band. If this represents an original crystal boundary within the parent calcite sample that separates two crystals with slightly different crystallographic orientations, twining and slip across it would be inhibited. Locally, the sample displays twin planes and evidence of glide near the boundary in the middle of the sample; these features are not planar and taper to tips. Twinning at the sample ends also is apparent locally. Because of the anomalous strength and presence of microstructural features that suggest it is not a single crystal, sample CIC5 was not analyzed further.

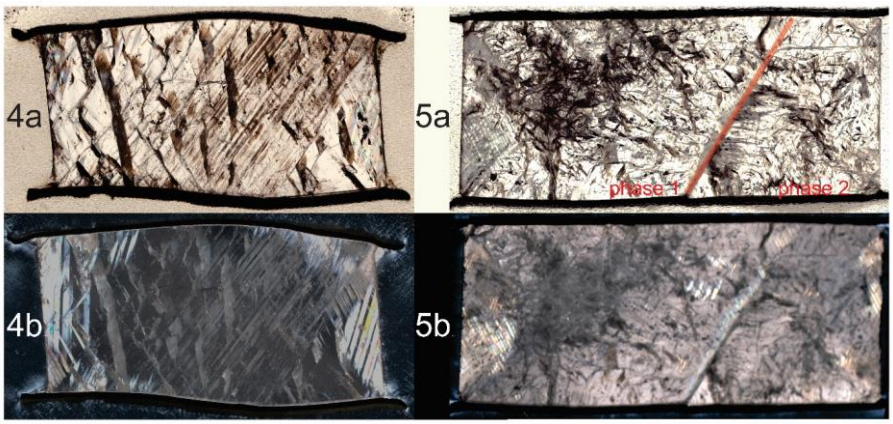

Figure 13. Scanned images of the CIC4 and CIC5 samples. 4a, b) Sample CIC4. Sa, b) Sample CIC5. Images (4a) and (5a) are plane-polarized light, and images (4b) and (5b) are cross-polarized light. The red line on (5a) shows the boundary of two phases of the calcite crystal.

The photograph of CIC6, which was loaded normal to the c-axis, displays a thick kink band through the central part of the sample (Fig. 14). Within the thick band are a couple parallel, thin kink bands (outlined with a red square and shown in the detail photo, Fig. 14). The broad shear band is recorded by both rotation of twin planes between the band boundaries relative to those within the sample ends, as well as the passive rotation of the sample sides. A high density of twin planes curve sharply to define the boundaries of the kink bands. The passive rotation of twins and the sample sides records a larger shear strain.

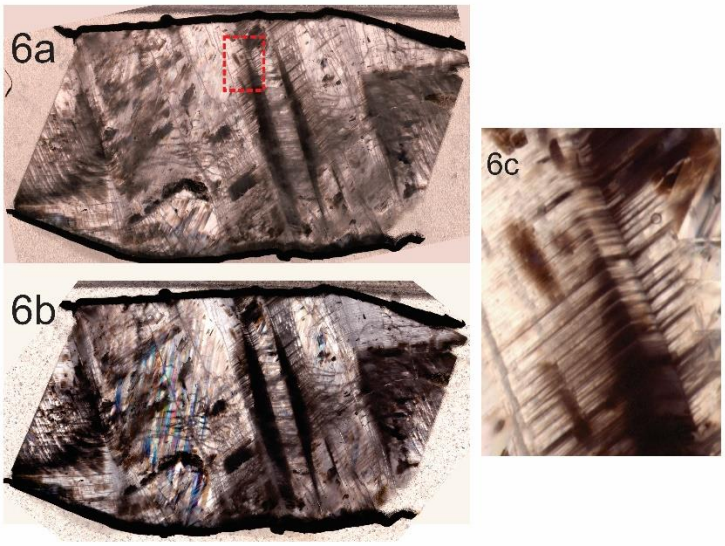

Figure 14. Scanned images of CIC6 sample under (6a) plane-polarized and (6b) cross-polarized light. The red square in (6a) marks the location of kink bands and the photograph in (6c).

Samples CIC6 and CIC7 were both loaded perpendicular to the c-axis, but CIC7 was deformed at a higher temperature of 200°C. The higher temperature of deformation of CIC7, and greater ductility, is reflected in the overall shape of the sample and in the microstructures (Fig. 15). Like CIC6, this sample shows a single broad kink band in the central potion, but is characterized by more gently curved twin planes at the kink boundaries. The twins are more

uniformly developed in CIC7 with no smaller scale kinking. At the center of the CIC7 thin section there is a relatively less deformed, lenticular segment that extends across the kink band parallel to the twin planes. This thin section also displays wider twinned zones at the sample ends, in contrast to zones of narrow twins in the central sheared region.

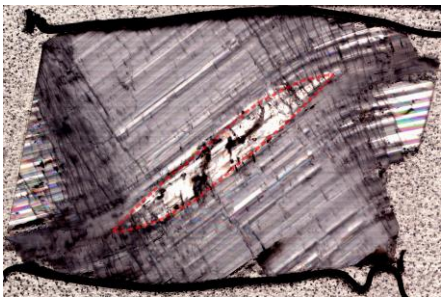

Figure 15. Scanned image of the CIC7 sample under cross-polarized light.

Crystallographic Orientation Determinations Using EBSD Data and e-Twin Sets

The EBSD data was used to confirm that the calcite crystals were in fact cored in the intended orientations relative to the core axis, and to determine the orientations of the *m* planes and *a* crystallographic axes. In addition, the EBSD data specifies the orientation of the petrographic thin section within each crystal relative to the crystallographic directions. To determine the original core sample orientation, EBSD measurement were collected near the core axis and near the ends of the cores adjacent to the piston, as these areas are most protected from large deformations that may have been introduced by the piston. Overall, the EBSD data document that the crystals were cored within a few degrees of the intended directions. EBSD data collected from numerous locations within the interior of the deformed samples provided information on magnitude of passive rotations of crystallographic axes, as well as the directions of the rotation axes. These data clearly record 1) rotation of the c-axes associated with mechanical e-twinning of 53˚, and 2) passive rotation of the c-axes in twinned and non-twinned

areas around the *a* axes, consistent with e-twinning and r-slip mechanisms. Passive rotations were also recorded by bent e-twins, particularly evident in samples CIC6 and CIC7, which are consistent with rotations determined using EBSD data.

Samples CIC1 and CIC2 were not inspected with EBSD techniques due to the difficulty in sectioning and polishing, which could not be redone due to limitations of remaining core sample volumes that needed to be retained for isotope analyses. However, both these samples displayed three sets of twins in the regions near the sample ends, which underwent passive rotations of less than a few degrees. As such, the orientations of the three sets of twin lines, formed by intersection of the twins with the plane of the petrographic section, could be used to determine uniquely the orientation of the crystallographic directions, as well as the orientation of the section with respect to the crystal orientations. This analysis confirmed the actual orientation of the core sample axes in CIC1 and CIC2 also were within a few degrees of the intended core orientation, and thus allowed for subsequent analyses of activated twin and slip systems in the interior of the samples experiencing the largest strains (Figs. 16-22).

DISCUSSION

Analysis of Activated Twin and Slip Systems

Using the planar deformation features evident in the optical photomicrographs along with knowledge of the orientation of the crystallographic directions, the load axis (core axis) direction, and the passive rotations of twin planes and the top and bottom boundaries of the deformed core samples, it is possible to identify the twin planes and the slip systems that were activated during deformation with good confidence. In some sample orientations (e.g., loaded normal to the c-axis) twin gliding in a single e-twin direction accommodated the majority of the sample shortening; in other cases multiple twin systems and slip systems were activated to different degrees to achieve the total strain (e.g., loaded parallel to the c-axis). The crystallographic orientations and the deformation features identified are illustrated in decorated photomicrographs of the sectioned samples, and in upper and lower hemisphere projections to the plane of each thin section. The projections include the crystallographic orientations defined by EBSD and the twin and slip planes and slip directions plotted in the thin section reference frame (Figs. 16-22).

Samples CIC1 and CIC2 show evidence of the activation of all three e-twin directions and multiple r^- slip directions. At the lower temperature of CIC1 deformation, the e-twinning is concentrated at the sample ends, near the piston. The wedge shape of the bulged region and shear in the central portion of the CIC1 sample likely reflect a combination of r^-_1, r^-_2, and r^-_3 slip. In contrast, at the higher temperature of deformation, shear in the central portion of the CIC2 sample appears as a single, wide band of shear achieved through a combination of e_1-twinning and r^-_1 slip. The twins in the shear band appear to have passively rotated towards the load axis by the e_1-twinning or by r^-_1 slip. Although the twins in the shear band are parallel to e_3-twinning

near the end of the sample, slip on e_3 is in-and-out of the thin section plane and therefore would not produce the shear strain in the band evidenced by rotation of the core sample boundaries. In this sample, the shear band boundary is parallel to the r^-_1 slip plane, but the magnitude and extent of r^-_1 slip is not known (Figs. 16 and 17).

The undeformed CIC3 core was shorter than desired for triaxial testing. A shorter dimension of cores in the load axis direction tends to produce a stronger sample, greater homogeneous barreling, and more complex deformation associated with strain constraints and piston friction effects. The sample displays faint planar deformation features, which combined with the crystallographic orientations, strongly suggest that the dominant twin direction is e_1 and that the dominant slip direction is r^+_1, with possible operation of r^+_2 as well (Fig. 18).

The CIC4 sample clearly displays the three e-twin planes within the sample ends and the three r^- slip bands within the central region of the sample. The parallel, closely spaced r^-_2 slip bands and passive rotation of the sample sides by shear on the r^-_2 bands suggests r^-_2 is the dominant strain producing slip plane in this sample (Fig. 19).

The CIC6 sample displays extensive e-twinning by e_1, but also planar bands parallel to r^+_3, and r^+_1 bands parallel to the kink-band boundaries. The twins are reoriented by passive rotation in the kink band, and EBSD crystallographic orientation measurements at many locations in the kink band records rotation of c-axes due to e-twinning, as well as the passive rotation of twin planes due to shear. Although slip on r^+_1 planes parallel to the kink band boundary could contribute to the shear observed across the kink band, it also is possible that the r^+_1 plane serves to accommodate the strain incompatibility at the kink band boundaries but does little to generate shear within the band (Fig. 21).

a.

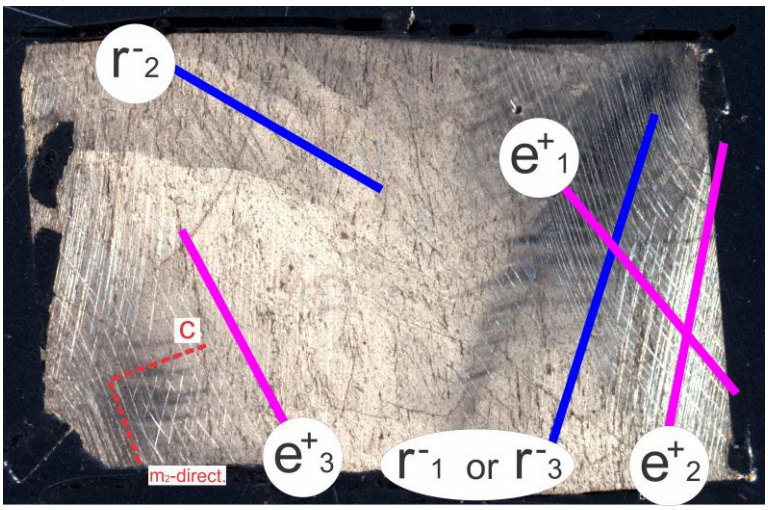

b.

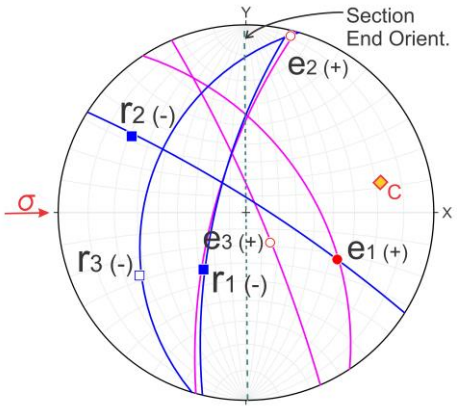

Slip and Twin
Systems of CIC1

Figure 16. Analysis of crystallographic axes and deformation of the sample from experiment CIC1. a) Photograph of the petrographic section of the deformed sample with labels of crystallographic directions (red lines, solid with arrowhead if in the plane of the section and dashed if not), and orientation of e-twin (pink) and r-glide (blue) planes. b) Orientation of interpreted twin (e+) and glide (r+, r-) planes that contributed to deformation of the sample relative to the orientation of the end of the sample (SEO), the load axis (σ), the crystallographic directions (e.g., c-axis), and the petrographic section coordinates (X, Y), in an equal-area projection onto the plane of the section. Great circles show the orientation of the e-planes (pink), r-planes (blue) with circles in corresponding colors indicating the slip direction. Note the open circles represent direction in the upper hemisphere, and solid circles represent the direction in the lower hemisphere, and that the great circles are in the same hemisphere corresponding to the slip direction.

CIC2

a.

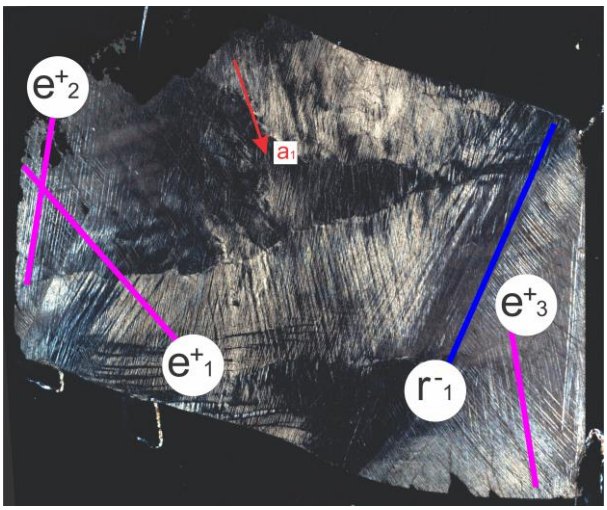

b.

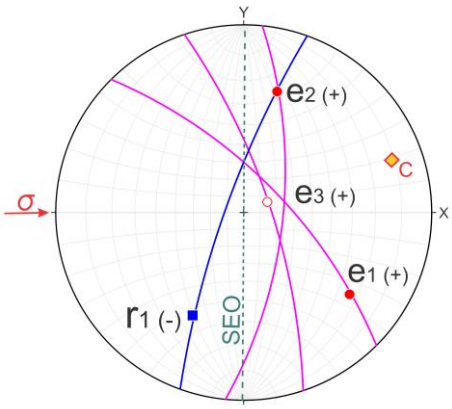

Slip and Twin Systems of CIC2

Figure 17. Analysis of crystallographic axes and deformation of the sample from experiment CIC2. a) Photograph of the petrographic section of the deformed sample with labels of crystallographic directions (red lines, solid with arrowhead if in the plane of the section and dashed if not), and orientation of e-twin (pink) and r-glide (blue) planes. b) Orientation of interpreted twin (e+) and glide (r+, r-) planes that contributed to deformation of the sample relative to the orientation of the end of the sample (SEO), the load axis (σ), the crystallographic directions (e.g., c-axis), and the petrographic section coordinates (X, Y), in an equal-area projection onto the plane of the section. Great circles show the orientation of the e-planes (pink), r-planes (blue) with circles in corresponding colors indicating the slip direction. Note the open circles represent direction in the upper hemisphere, and solid circles represent the direction in the lower hemisphere, and that the great circles are in the same hemisphere corresponding to the slip direction.

CIC3

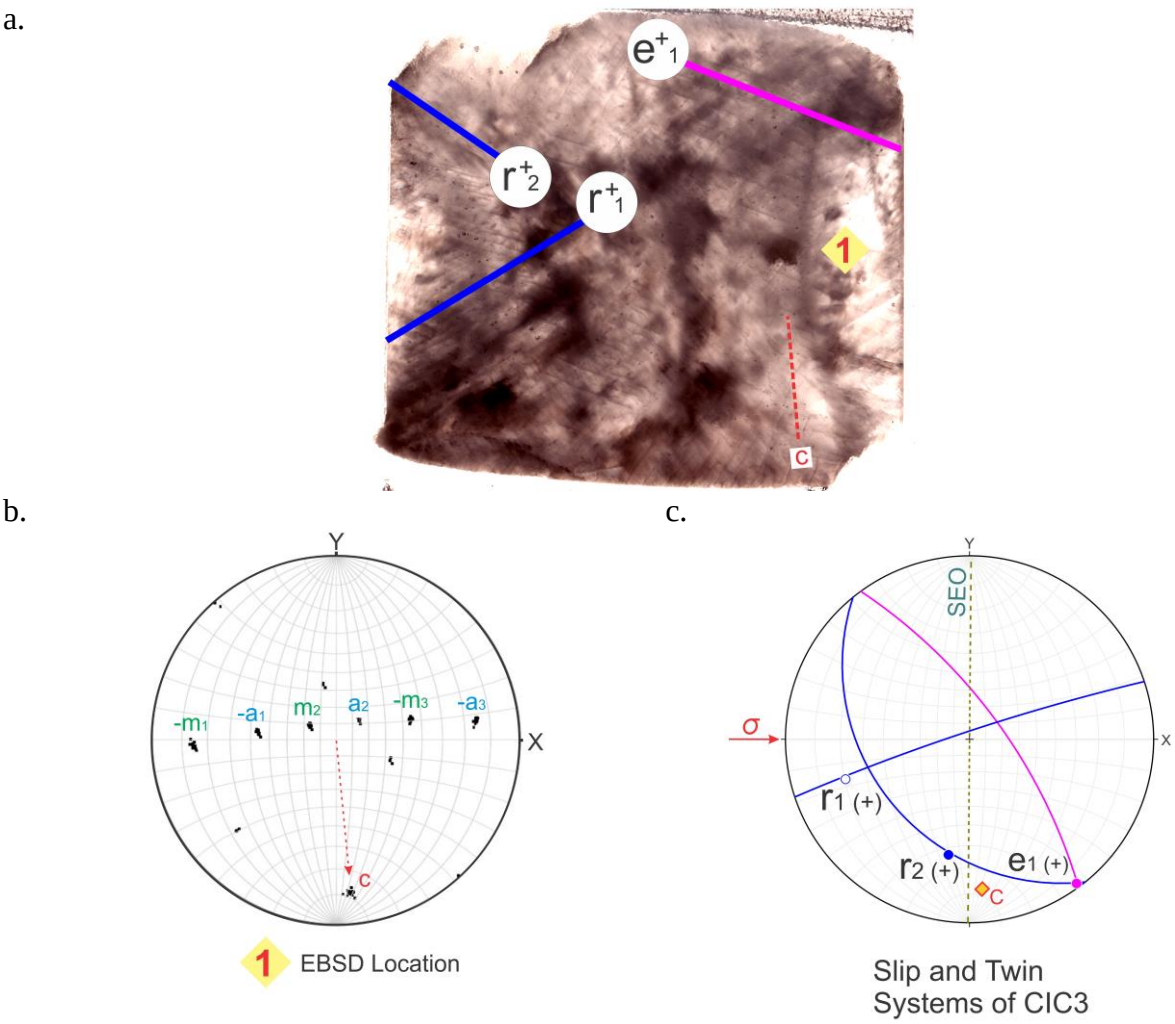

Figure 18. Analysis of crystallographic axes and deformation of the sample from experiment CIC3. a) Photograph of the petrographic section of the deformed sample with labels of crystallographic directions (red lines, solid with arrowhead if in the plane of the section and dashed if not), EBSD measurement location (yellow diamond), and orientation of e-twin (pink) and r-glide (blue) planes. b) Crystallographic axes determined from EBSD measurement in the location keyed to the photograph, and shown in an upper-hemisphere, equal-angle projection to the plane of the petrographic section with the X-direction to the right, parallel to the long axis of the petrographic section. c) Orientation of interpreted twin (e+) and glide (r+, r-) planes that contributed to deformation of the sample relative to the orientation of the end of the sample (SEO), the load axis (σ), the crystallographic directions (e.g., c-axis), and the petrographic section coordinates (X, Y), in an equal-area projection onto the plane of the section. Great circles show the orientation of the e-planes (pink), r-planes (blue) with circles in corresponding colors indicating the slip direction. Note the open circles represent direction in the upper hemisphere, and solid circles represent the direction in the lower hemisphere, and that the great circles are in the same hemisphere corresponding to the slip direction.

a.

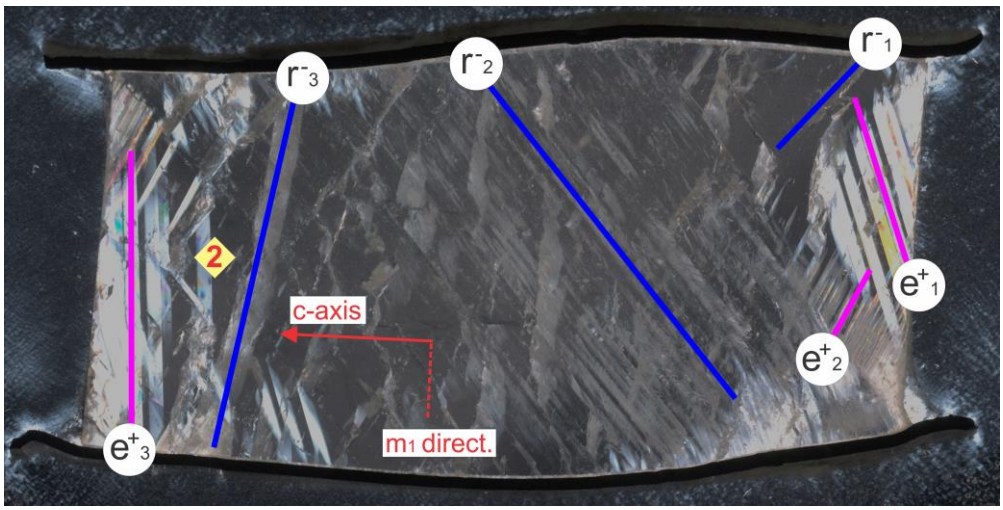

b.

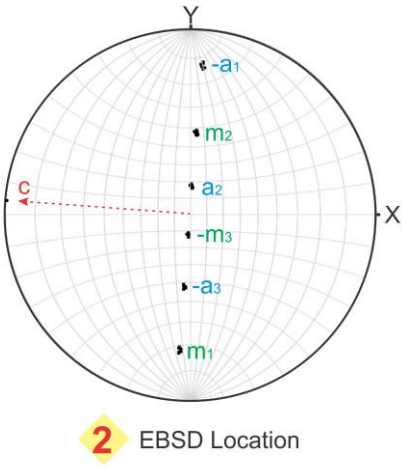

c.

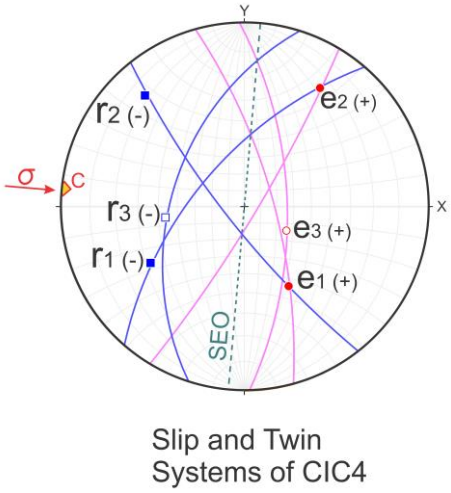

Figure 19. Analysis of crystallographic axes and deformation of the sample from experiment CIC4. a) Photograph of the petrographic section of the deformed sample with labels of crystallographic directions (red lines, solid with arrowhead if in the plane of the section and dashed if not), EBSD measurement location (yellow diamond), and orientation of e-twin (pink) and r-glide (blue) planes. b) Crystallographic axes determined from EBSD measurement in the location keyed to the photograph, and shown in an upper-hemisphere, equal-angle projection to the plane of the petrographic section with the X-direction to the right, parallel to the long axis of the petrographic section. c) Orientation of interpreted twin (e+) and glide (r+, r-) planes that contributed to deformation of the sample relative to the orientation of the end of the sample (SEO), the load axis (σ), the crystallographic directions (e.g., c-axis), and the petrographic section coordinates (X, Y), in an equal-area projection onto the plane of the section. Great circles show the orientation of the e-planes (pink), r-planes (blue) with circles in corresponding colors indicating the slip direction. Note the open circles represent direction in the upper hemisphere, and solid circles represent the direction in the lower hemisphere, and that the great circles are in the same hemisphere corresponding to the slip direction.

a.

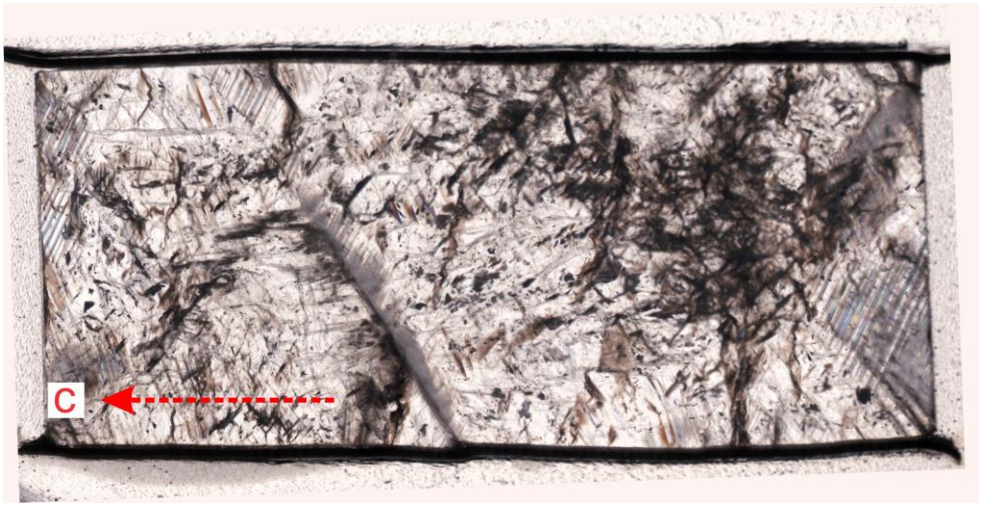

b.

c.

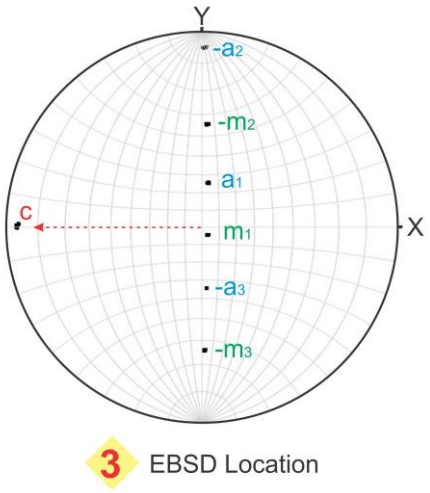

Figure 20. Analysis of crystallographic axes of the sample from experiment CIC5. Deformation features are not interpreted for this experiment as explained in the text. a) Photograph of the petrographic section of the deformed sample with labels of crystallographic directions (red lines, solid with arrowhead if in the plane of the section and dashed if not). b) Crystallographic axes determined from EBSD measurement in the location keyed to the photograph, and shown in an upper-hemisphere, equal-angle projection to the plane of the petrographic section with the X-direction to the right, parallel to the long axis of the petrographic section.

CIC6

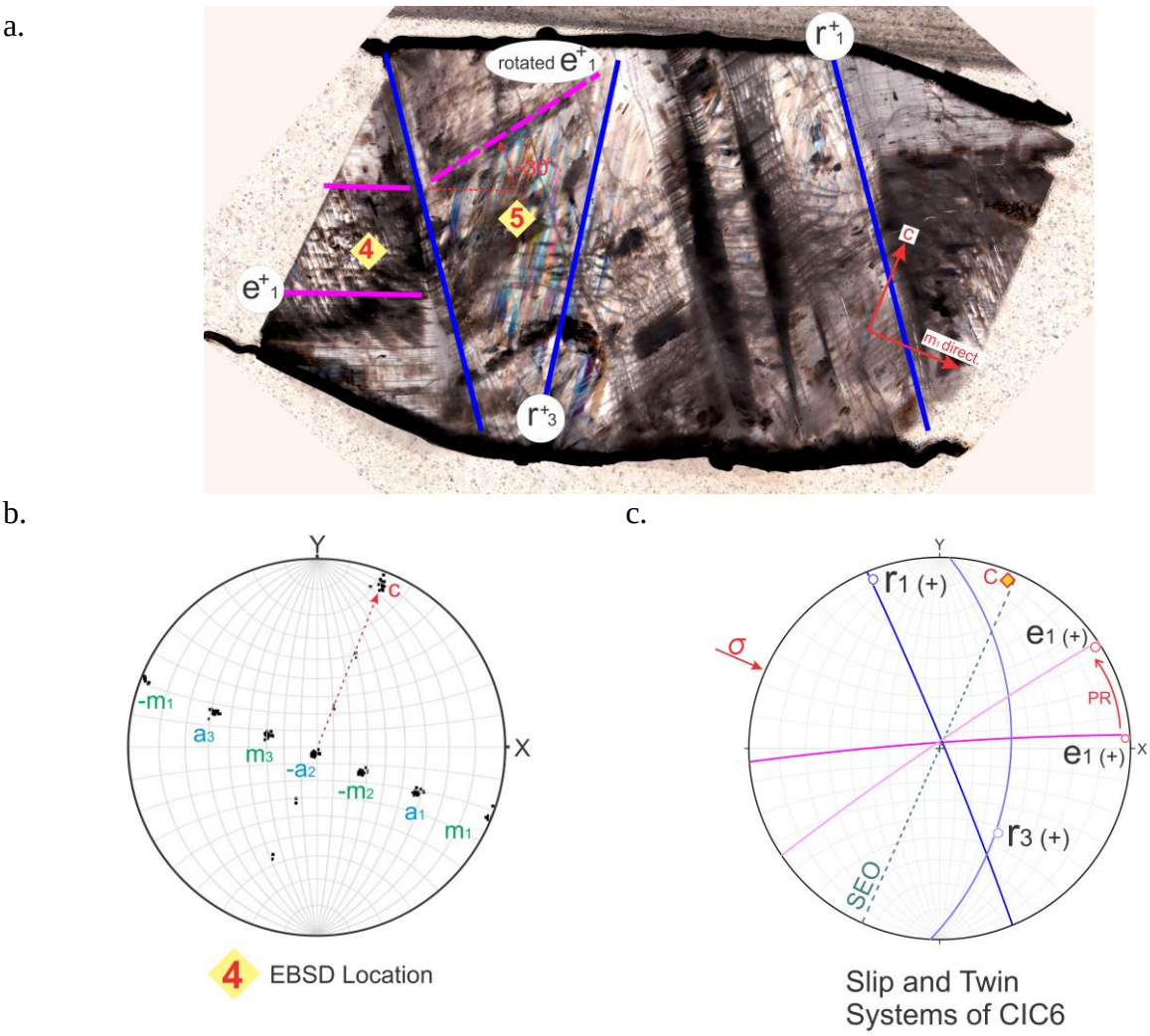

Figure 21. Analysis of crystallographic axes and deformation of the sample from experiment CIC6. a) Photograph of the petrographic section of the deformed sample with labels of crystallographic directions (red lines, solid with arrowhead if in the plane of the section and dashed if not), EBSD measurement location (yellow diamond), and orientation of e-twin (pink) and r-glide (blue) planes. b) Crystallographic axes determined from EBSD measurement in the location keyed to the photograph, and shown in an upper-hemisphere, equal-angle projection to the plane of the petrographic section with the X-direction to the right, parallel to the long axis of the petrographic section. c) Orientation of interpreted twin (e+) and glide (r+, r-) planes that contributed to deformation of the sample relative to the orientation of the end of the sample (SEO), the load axis (σ), the crystallographic directions (e.g., c-axis), and the petrographic section coordinates (X, Y), in an equal-area projection onto the plane of the section. Great circles show the orientation of the e-planes (pink), r-planes (blue) with circles in corresponding colors indicating the slip direction. Note the open circles represent direction in the upper hemisphere, and solid circles represent the direction in the lower hemisphere, and that the great circles are in the same hemisphere corresponding to the slip direction.

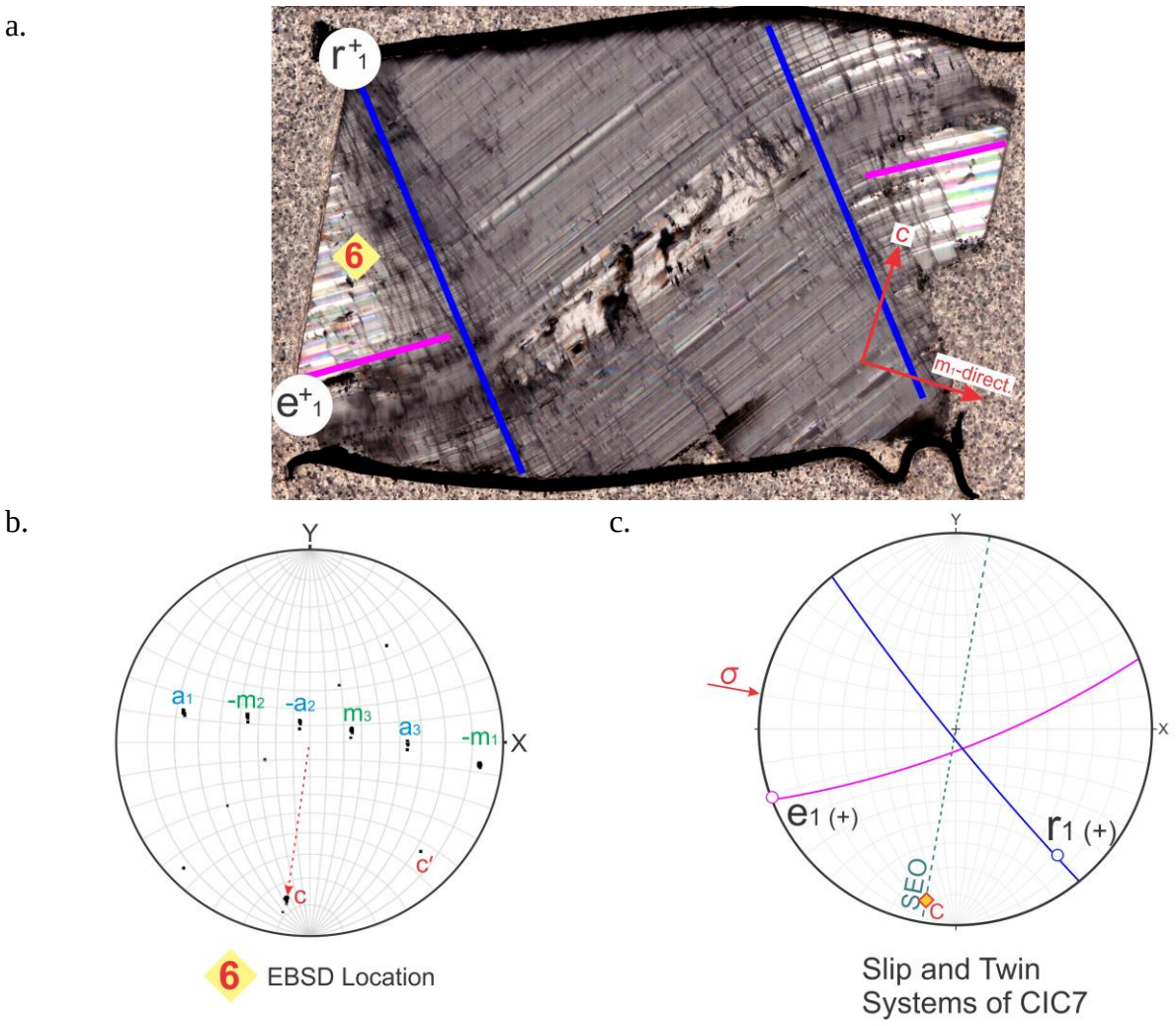

Figure 22. Analysis of crystallographic axes and deformation of the sample from experiment CIC6. a) Photograph of the petrographic section of the deformed sample with labels of crystallographic directions (red lines, solid with arrowhead if in the plane of the section and dashed if not), EBSD measurement location (yellow diamond), and orientation of e-twin (pink) and r-glide (blue) planes. b) Crystallographic axes determined from EBSD measurement in the location keyed to the photograph, and shown in an upper-hemisphere, equal-angle projection to the plane of the petrographic section with the X-direction to the right, parallel to the long axis of the petrographic section. c) Orientation of interpreted twin (e+) and glide (r+, r-) planes that contributed to deformation of the sample relative to the orientation of the end of the sample (SEO), the load axis (σ), the crystallographic directions (e.g., c-axis), and the petrographic section coordinates (X, Y), in an equal-area projection onto the plane of the section. Great circles show the orientation of the e-planes (pink), r-planes (blue) with circles in corresponding colors indicating the slip direction. Note the open circles represent direction in the upper hemisphere, and solid circles represent the direction in the lower hemisphere, and that the great circles are in the same hemisphere corresponding to the slip direction.

The CIC7 sample is geometrically very similar to the deformation in the CIC6 sample, but the e_1 twins are very well developed and likely produce the bulk of the shear strain in the kink band. There are, however, a number of planar features in the boundary regions of the kink that roughly parallel r^+_1 planes, so similar to CIC5 some shear strain may be produced by activation of r^+_1 slip but is it likely subordinate.

Deformation and Yield Strength

As a result of having very good information on the orientation of the crystallographic axes for each deformed sample, it is possible to call on the relatively well documented critical resolved shear stress determinations for twin and slip systems in calcite from previous work (e.g., Turner, 1954; De Bresser and Spiers, 1997; Table 3) to calculate the expected yield stress to activate slip for each deformed sample. This is done to independently check the likelihood of activating the twin and slip planes if the deformed samples.

Table 3. Critical Resolved Shear Stress* for Twin and Slip

Temperature (°C)	e-twin	r^- slip	r^+ slip
20	5.5	196	180
200	2.9	42	60
400	1.6	12	22

*Values determined from work by Turner (1954) and De Bresser and Spiers (1997).

Table 4 presents the calculated Schmid factors for each e-twin, r^- slip, and r^+ slip plane based on the load direction relative to the slip plane and slip direction. The differential stress for activation of each twin and slip plane is determined from the quotient of the critical resolved shear stress by the Schmid factor. Table 5 provides the observed yield and final stress measured during deformation of each sample, compared to the calculated stress for each twin and slip plane. The twin and slip planes identified in each deformed sample are identified by red

underline in table 5 for easy comparison. In general, the observed yield and final stresses are similar to the calculated stresses for the identified twin and slip planes, though in some cases very high calculated stress for some slip planes may be taken as arguments that those slip planes were not significant or misidentified.

For example, in CIC6 and CIC7 samples, the observed yield stress is low and some work hardening is observed. The stress levels are clearly similar to the activation of e_1-twinning. The stress for activating r^+_1, which was inferred from observed planar features, is extremely high by comparison and thus would seem unlikely to have been activated except only very locally. In these samples the observed work hardening is more likely explain as a consequence of passive rotation of the potential e_1-twin plane decreasing the Schmid factor and raising the stress necessary for continued twining in the band.

In contrast, the observed initial yield and final stress in samples CIC1 and CIC4 are fairly high thus could explain the activation of all three e-twin planes and all three r^- slip planes as is clearly observed in the CIC4 sample and inferred for CIC1sample. The observed twin and slip planes activated in CIC3 and the observed yield and final stress also are consistent with the yield stress calculated for these plans.

Table 4. Schmid Factors for Twin and Slip Planes in Experiments

Load Orientation	$\mathbf{e_1}^+$	$\mathbf{e_2}^+$	$\mathbf{e_3}^+$	$\mathbf{r_1}^-$	$\mathbf{r_2}^-$	$\mathbf{r_3}^-$	$\mathbf{r_1}^+$	$\mathbf{r_2}^+$	$\mathbf{r_3}^+$
22° to c-axis	0.49	0.22	0.22	-0.37	-0.47	-0.47	0.37	0.42	0.42
68° to c-axis	-0.5	-0.02	-0.02	0.4	0.07	0.07	-0.4	-0.07	-0.07
// to c-axis	0.35	0.42	0.42	-0.5	-0.5	-0.5	0.5	0.5	0.5
normal to c-axis	-0.386	-0.1	-0.1	0.49	0.12	0.12	-0.49	-0.12	-0.12

Table 5. Comparison of Observed and Calculated Yield Strengths

Exp. #	T (°C)	Observed Yield σ (MPa)	Observed Final σ (MPa)	e_1^+	e_2^+	e_3^+	r_1^-	r_2^-	r_3^-	r_1^+	r_2^+	r_3^+
CIC1	200	24	65	6	13	13	114	89	89	162	143	143
CIC2	400	~8	~13	3	7	7	32	26	26	59	52	52
CIC3	200	23	68	6	145	145	105	600	600	150	857	857
CIC4	20	60	89	16	13	13	392	392	392	360	360	1500
CIC5	200	172	288	8	7	7	84	84	84	120	120	120
CIC6	20	7	25	14	55	55	1633	1633	1633	367	1500	1500
CIC7	200	5	17	8	29	29	84	350	350	122	500	500

Recommendations and Expected Outcomes for Clumped Isotope Analysis of Deformed Samples

The suite of experiments provides good opportunity to identify if any of the lower temperature (<200˚C) twin and slip systems can cause changes in clumped isotope signatures. For example, samples CIC6 and CIC7 provide domains of calcite (within the kink bands) deformed primarily by e-twinning to large shear strain, and thus isolating the e-twin mechanism. Sample CIC4 provides a domain in which large strain is achieved by operation of the r^- slip system (all three planes) without significant twinning, and thus allowing isolation of the r^- slip mechanism. Sample CIC3 provides the best opportunity to investigate the role of r^+ slip on isotopes as it is highly deformed at high stress by a combination of e-twinning and r^+ slip. Finally, samples CIC1 and CIC2 both deform by combined e-twinning and multiple r^- slip planes. Thus, samples CIC1, CIC2 and CIC3 allow investigation of whether complex interaction of various twin and slip systems affects clumped isotope signatures.

As Reeder (1983) discussed, the strength of a C-O bond is greater than the strength of a Ca-O bond. This means that a Ca-O bond requires higher pressure to be broken during deformation. At this point, the Schmid factors calculated with respect to two applied stress directions would be useful for having an idea about types of broken bonds during experiments. In such a way that

high Schmid factor values of deformation mechanisms in calcite could be associated with breaking of C-O bonds and if we could break C-O bonds, a new equilibrium of isotope distribution would be adjusted according to the temperature existing during deformations. This could prove that deformation has an influence on clumped isotope signature of calcite by means of breaking the C-O bonds and establishing a new equilibrium of isotopic distribution in compliance with deformation temperature.

In case of absence of changed Δ_{47} values, we may think of two likely interpretations. Unmodified Δ_{47} values would imply that there are no C-O bonds being broken during deformation. Thus, the internal equilibrium of isotopic distribution would stay undisrupted in calcite. Even if we could break the C-O bonds and disrupt the equilibrium, we still would be unable to see any change in clumped isotope measurements due to lack of required time for resetting and establishing new internal equilibrium in calcite. In both cases, we may not see any new, post-deformation Δ_{47} measurements.

CONCLUSIONS

- This study involves a key contribution to the important scientific question of whether low- to moderate-temperature deformation of calcite can change the signature of clumped isotopes, which are frequently used as a paleothermometer in geologic and environmental studies.
- Experimental deformation of single crystal calcite samples was completed to allow direct measurements of clumped isotope concentrations in deformed and undeformed calcite from the same parent calcite crystal, thus verifying whether deformation affects clumped isotopes in calcite.
- Analysis of the deformation in the experimentally deformed crystals identifies the active deformation processes of e-twinning, r^+ slip, and r^- slip. An important outcome is that some domains of the deformed samples are identified in which only e-twinning operates, only r- slip operates, combined r+ slip and e-twinning operates, or combined r- and e-twinning operates, which allows a means to identify if any individual mechanism, or combination of mechanisms, can affect clumped isotopes.
- Follow-up work by experts in clumped isotope analysis will use the products of this study to confirm if clumped isotopes are affected by low temperature deformation. Any outcome will be useful to the community using clumped isotopes for paleothermometry, and as well to efforts to understand the fundamental, atomic-scale processes of mechanical twinning and slip by dislocation motion.

REFERENCES

Affek, H.P., 2012. Clumped isotope paleothermometry: principles, applications, and challenges. In: Ivany, L.C., Huber, B. (Eds.), Reconstructing Earth's Deep-Time Climate —The State of the Art in 2012. Paleontological Society Papers, pp. 101–114.

Bigeleisen, J. (1955). Statistical mechanics of isotopic systems with small quantum corrections. I. General considerations and the rule of the geometric mean. The Journal of Chemical Physics, 23(12), 2264-2267.

Borg, I., & Handin, J. (1967). Torsion of calcite single crystals. Journal of Geophysical Research, 72(2), 641-669.

De Bresser, J. H. P., & Spiers, C. J. (1990). High-temperature deformation of calcite single crystals by r+ and f+ slip. Geological Society, London, Special Publications, 54(1), 285-298.

De Bresser, J. H. P. (1991). Intracrystalline deformation of calcite (Doctoral dissertation, Instituut voor Aardwetenschappen der Rijksuniversiteit Utrecht).

De Bresser, J. H. P., & Spiers, C. J. (1993). Slip systems in calcite single crystals deformed at 300–800 C. Journal of Geophysical Research: Solid Earth, 98(B4), 6397-6409.

De Bresser, J. H. P., & Spiers, C. J. (1997). Strength characteristics of the r, f, and c slip systems in calcite. Tectonophysics, 272(1), 1-23.

Dennis, K. J., and D. P. Schrag (2010), Clumped isotope thermometry of carbonatites as an indicator of diagenetic alteration, Geochim. Cosmochim. Acta., 74(14), 4110-4122.

Eagle, R. A., T. Tütken, T. S. Martin, A. K. Tripati, H. C. Fricke, M. Connely, R. L. Cifelli, and J. M. Eiler (2011), Dinosaur body temperatures determined from isotopic (13C-18O) ordering in fossil biominerals, Science, 333(6041), 443-445.

Eiler, J. M., & Schauble, E. (2004). 18 O 13 C 16 O in Earth's atmosphere. Geochimica et Cosmochimica Acta, 68(23), 4767-4777.

Eiler, J.M., 2007. "Clumped-isotope" geochemistry—the study of naturally-occurring, multiply substituted isotopologues. Earth Planet. Sci. Lett. 262, 309–327.

Eiler, J.M., 2011. Paleoclimate reconstruction using carbonate clumped isotope thermometry. Quat. Sci. Rev. 30, 3575–3588.

Finnegan, S., K. Bergmann, J. M. Eiler, D. S. Jones, D. A. Fike, I. Eisenman, N. C. Hughes, A. K. Tripati, and W. W. Fischer (2011), The magnitude and duration of late Ordovician-early Silurian glaciation, Science, 331(6019), 903-906.

Friedman, M., & Conger, F. B. (1964). Dynamic interpretation of calcite twin lamellae in a naturally deformed fossil. The Journal of Geology, 72(3), 361-368.

Ghosh, P., Adkins, J., Affek, H., Balta, B., Guo, W., Schauble, E. A., ... & Eiler, J. M. (2006). 13 C–18 O bonds in carbonate minerals: A new kind of paleothermometer. Geochimica et Cosmochimica Acta, 70(6), 1439-1456.

Griggs, D. T., Turner, F. J., & Heard, H. C. (1960). Deformation of Rocks at 500° to 800° C. Geological Society of America Memoirs, 79, 39-104.

Heard, H. C., & Carter, N. L. (1968). Experimentally induced natural intragranular flow in quartz and quartzite. American Journal of Science, 266(1), 1-42.

Huntington, K.W. and Lechler, A. R., 2015. Carbonate clumped isotope thermometry in continental tectonics. Tectonophysics 647–648 (2015) 1–20

Lloyd, M. K., Eiler, J. M., &Nabelek, P. I. (2017). Clumped isotope thermometry of calcite and dolomite in a contact metamorphic environment. Geochimica et Cosmochimica Acta, 197, 323-344.

Luetkemeyer, P. B., Kirschner, D. L., Huntington, K. W., Chester, J. S., Chester, F. M., & Evans, J. P. (2016). Constraints on paleofluid sources using the clumped-isotope thermometry of carbonate veins from the SAFOD (San Andreas Fault Observatory at Depth) borehole. Tectonophysics.

McKinney, C. R., McCrea, J. M., Epstein, S., Allen, H. A., & Urey, H. C. (1950). Improvements in mass spectrometers for the measurement of small differences in isotope abundance ratios. Review of Scientific Instruments, 21(8), 724-730.

Quade, J., Breecker, D. O., Daëron, M., & Eiler, J. (2011). The paleoaltimetry of Tibet: An isotopic perspective. American Journal of Science, 311(2), 77-115.

Paterson, M. S., & Turner, F. J. (1970). Experimental deformation of constrained crystals of calcite in extension. In Experimental and Natural Rock Deformation/Experimentelle und natürliche Gesteinsverformung (pp. 109-141). Springer, Berlin, Heidelberg.

Reeder, R. J. (1983). Crystal chemistry of the rhombohedral carbonates. Reviews in Mineralogy and Geochemistry, 11(1), 1-47.

Richet, P., Bottinga, Y., & Javoy, M. (1977). A review of hydrogen, carbon, nitrogen, oxygen, sulphur, and chlorine stable isotope fractionation among gaseous molecules. Annual Review of Earth and Planetary Sciences, 5(1), 65-110.

Rowe, K. J., & Rutter, E. H. (1990). Palaeostress estimation using calcite twinning: experimental calibration and application to nature. Journal of Structural Geology, 12(1), 1-17.

Rybacki, E., Evans, B., Janssen, C., Wirth, R., & Dresen, G. (2013). Influence of stress, temperature, and strain on calcite twins constrained by deformation experiments. Tectonophysics, 601, 20-36.

Schuster, R., Schafler, E., Schell, N., Kunz, M., & Abart, R. (2017). Microstructure of calcite deformed by high-pressure torsion: An X-ray line profile study. Tectonophysics, 721, 448-461.

Spiers, C. J., & Wenk, H. R. (1980). Evidence for slip on r and f in the positive sense in deformed calcite single crystals. Transactions American Geophysical Union, 3(2), 1128

Suarez, M. B., B. H. Passey, and A. Kaakinen (2011), Paleosol carbonate multiple isotopologue signature of active East Asian summer monsoons during the late Miocene and Pliocene, Geology, 39(12), 1151-1154.

Swanson, E. M., B. P. Wernicke, J. M. Eiler, and S. Losh (2012), Temperatures and fluids on faults based on carbonate clumped-isotope thermometry, Am. J. Sci., 312(1), 1-21.

Turner, F. J. (1954). Deformation twinning on $\{10\bar{1}1\}$ and $\{02\bar{2}1\}$in experimentally deformed calcite. Mineralogy and Petrology, 4(1), 28-33.

Turner, F. J., Griggs, D. T., Heard, H. (1954). Experimental deformation of calcite crystals. Geological Society of America Bulletin, 65(9), 883-934.

Turner, F. J., & Orozco, M. (1976). Crystal bending in metamorphic calcite, and its relations to associated twinning. Contributions to Mineralogy and Petrology, 57(1), 83-97.

Weiss, L. E., & Turner, F. J. (1972). Some observations on translation gliding and kinking in experimentally deformed calcite and dolomite. Flow and Fracture of Rocks, 95-107.